Kinetic Energy Spectra and Spectral Budget of Radiative–Convective Equilibrium

KWAN TSAAN LAI[a] AND MICHAEL L. WAITE[a]

[a] *Department of Applied Mathematics, University of Waterloo, Waterloo, Ontario, Canada*

ABSTRACT: The atmospheric kinetic energy spectrum and energy cascade are investigated in idealized simulations of radiative–convective equilibrium (RCE). WRF is employed to perform cloud-resolving simulations of an idealized radiative–convective equilibrium with and without aggregation with $\Delta x = 4$ km. The horizontal kinetic energy (HKE) spectrum for the aggregated simulation in the upper troposphere is steeper than the nonaggregated case and closer to $-5/3$. The HKE spectra for the nonaggregated simulation in the upper troposphere and the lower stratosphere are much shallower than the $-5/3$ spectrum. In the upper troposphere, the divergent kinetic energy has a similar magnitude to the rotational kinetic energy in both the nonaggregated simulation and aggregated simulation. Energy is mainly gained from the buoyancy flux and mainly lost from the vertical energy flux for scales larger than 20 km. Downscale energy transfer is found in the upper troposphere. Numerical dissipation is the main source of energy loss at small scales. In the lower stratosphere, the divergent kinetic energy dominates the kinetic energy spectrum in both simulations. Energy is mainly gained from the vertical energy flux and is balanced by the loss from the buoyancy flux term, transfer term, and dissipation. An Eliassen–Palm flux analysis suggests that wave–mean-flow interaction may be responsible for the upscale energy transfer found in the lower stratosphere. The magnitudes of our kinetic energy spectra are similar to spectra calculated from aircraft data. Rotation is found to promote aggregation and steepen the energy spectrum.

KEYWORDS: Radiative-convective equilibrium; Numerical weather prediction/forecasting; Spectral analysis/models/distribution; Kinetic energy

1. Introduction

Radiative–convective equilibrium (RCE) is an idealized climate system driven by sensible and latent heat fluxes at the surface (e.g., Nolan et al. 2007; Wing et al. 2018). It is often considered as one of the simplest climate model configurations (e.g., Wing et al. 2018). We study the kinetic energy spectrum and spectral budget in simulations of RCE. A $-5/3$ kinetic energy spectrum has been identified from wavelengths of a few hundred km to small scales in both midlatitudes (e.g., Nastrom and Gage 1985) and the tropics (e.g., Cho et al. 1999). This spectrum is significant because $-5/3$ is the theoretical slope of a kinetic energy cascade, which suggests that an energy cascade may be occurring through the mesoscale. While the $-5/3$ kinetic energy spectrum has also been found in mesoscale simulations (e.g., Skamarock 2004; Peng et al. 2014; Sun et al. 2017) and global simulations (e.g., Hamilton et al. 2008; Skamarock et al. 2014; Malardel and Wedi 2016), the responsible physical mechanisms are still unclear.

Whether RCE will generate the $-5/3$ mesoscale spectrum is uncertain. RCE is at a statistical equilibrium and is driven by surface fluxes rather than baroclinic instability, which is different from most other idealized simulations of the mesoscale spectrum. Unlike midlatitude simulations, in which KE is forced at the large scales by baroclinic instability, KE in RCE is forced by surface fluxes and radiative cooling, and the characteristic length scales of this forcing is not clear. One interesting aspect of RCE is the phenomenon of self-aggregation (e.g., Bretherton et al. 2005; Wing and Emanuel 2014). Self-aggregation is the

organization of some small random cloud clusters into one or several larger clusters. Self-aggregation is known to be sensitive to subgrid parameterization and domain size (e.g., Bretherton et al. 2005; Wing and Emanuel 2014; Tompkins and Semie 2017). The effect of self-aggregation on the kinetic energy spectrum and energy cascade is still unknown. The fact that self-aggregation organizes small cloud clusters into large cloud clusters may affect how kinetic energy transfers from small scale to large scale in an inverse energy cascade. This connection between aggregation and the spectral budget is explored in this work.

a. RCE and self-aggregation

RCE is often used in model development and model comparison due to its simple configuration. In particular, it is used as a framework for understanding subgrid representations such as convective parameterizations (e.g., Becker et al. 2017) and cloud microphysics parameterizations (e.g., Satoh and Matsuda 2009). Since RCE generates a flow with many interacting convective systems at different scales, it has been employed in models with different horizontal resolutions such as atmospheric general circulation models (e.g., Reed and Medeiros 2016) and cloud-resolving models (e.g., Muller and Held 2012; Wing et al. 2017).

Self-aggregation is a phenomenon in which many small and random moist convective cores organize into a small number of large and isolated clusters (e.g., Wing et al. 2017). Self-aggregation in simulations is known to be sensitive to details of clouds parameterization (e.g., Satoh and Matsuda 2009), microphysics (e.g., Colin et al. 2019), circulations (e.g., Muller and Bony 2015), cold pool (e.g., Jeevanjee and Romps 2013), sea surface temperature (SST) (e.g., Bretherton et al. 2005; Wing et al. 2017), background wind (e.g., Robe and Emanuel

2001; Nolan et al. 2007), horizontal resolution (e.g., Bretherton et al. 2005; Muller and Held 2012), and domain size (e.g., Bretherton et al. 2005; Wing et al. 2017). Here, we review the literature to help us to understand the mechanisms and the importance of self-aggregation.

The resolution dependence of self-aggregation in RCE in Muller and Held (2012) was found to be related to the strength of the subgrid turbulence mixing by Tompkins and Semie (2017). They performed an investigation of the role of updraft entrainment on self-aggregation. In particular, they performed idealized RCE simulations with 2D Smagorinsky, 3D Smagorinsky, and turbulence kinetic energy (TKE) subgrid turbulence mixing scheme. They found that when the 3D Smagorinsky scheme was used, self-aggregation occurred. When a less dissipative subgrid turbulence mixing scheme such as the TKE scheme was used, there was no aggregation. However, by increasing the strength of the eddy viscosity of the TKE scheme, they recovered aggregation. This finding suggested that the strength of the eddy viscosity played a crucial role in self-aggregation in RCE. They further investigated the role of momentum and moisture subgrid mixing and found that when moisture subgrid mixing was neglected, there was no aggregation. They pointed out that entrainment was one of the main factors to whether the convective plumes aggregated or not.

Wing and Emanuel (2014) performed a budget analysis of the variance of the density-weighted, vertically integrated frozen moist static energy (FMSE) to identify the physical mechanisms associated with self-aggregation. When there is aggregation, the domain is separated into a dry and several moist regions. Since the moisture profile of the dry and moist regions are both significantly different from the mean moisture profile when there is aggregation, increased variance of FMSE can identify self-aggregation. Horizontal convergence feedback was found to be positive at the intermediate stage of the self-aggregation process, which was consistent with the circulation theory suggested by Bretherton et al. (2005) and Muller and Held (2012). Wing and Emanuel (2014) also found that air–sea disequilibrium feedback was strongly negative, and it was competing with strong positive feedback from the surface wind. They found that while longwave radiative cooling created positive feedback for self-aggregation at the early stage, it also created slightly weaker negative feedback for self-aggregation at the intermediate and late stages.

b. Energy spectrum

In this work, we investigate whether the $-5/3$ mesoscale kinetic energy spectrum develops in RCE and analyze the mechanisms that govern the energy at different length scales. The $-5/3$ kinetic energy spectrum has been reproduced in several idealized mesoscale simulations (e.g., Peng et al. 2014; Skamarock 2004; Sun et al. 2017). Unlike other mesoscale systems, where baroclinic instability controls large scales, mesoscale energy in RCE is generated entirely by the heating from surface fluxes and radiative cooling. These processes are not necessarily restricted to large scales, and so the resulting spectral budget may be more complicated than a cascade from large to small scales.

In a turbulent inertial range, energy is transferred conservatively between scales with a constant spectral flux. In this framework, dimensional arguments yield the Kolmogorov spectrum with a $-5/3$ slope (Kolmogorov 1941). Atmospheric measurements show a k_h^{-3} energy spectrum for synoptic scales in midlatitudes and a shallower $k_h^{-5/3}$ energy spectrum in the mesoscale (e.g., Nastrom and Gage 1985; Callies et al. 2014; Cho and Lindborg 2001) in tropics and midlatitudes, where k_h is the horizontal wavenumber. While there is a general agreement that the k_h^{-3} spectrum is due to quasigeostrophic turbulence (Charney 1971), there is no agreement on the mechanisms responsible for the $k_h^{-5/3}$ spectrum in the mesoscale. Proposed theories that attempted to explain the $k_h^{-5/3}$ spectrum fall into two categories: the direct energy cascade theory and inverse energy cascade theory (e.g., Lilly 1983). The inverse cascade hypothesis is found to be unlikely at scales smaller than 100 km (e.g., Cho and Lindborg 2001). Possible mechanisms for a downscale cascade include inertia–gravity waves (IGW) (e.g., VanZandt 1982; Callies et al. 2016), quasigeostrophic turbulence (e.g., Tung and Orlando 2003; Tulloch and Smith 2009), and strongly stratified turbulence (e.g., Lindborg 2006).

c. Energy spectral budget

Classical turbulence theories assume that there is no significant source or sink of kinetic energy in the inertial subrange between the forcing and dissipation scales. As a result, cascade theories of the mesoscale energy spectrum implicitly make this assumption. However, moist processes can energize the mesoscale by directly injecting energy at the mesoscale according to Waite and Snyder (2013). They investigated the effect of moisture on the mesoscale KE spectrum in a baroclinic wave. The buoyancy flux spectrum suggested that the energy generated by latent heat injected kinetic energy at the mesoscale.

Augier and Lindborg (2013) developed a formulation for spectral energy budget analysis to compare two hydrostatic global numerical weather forecasting models: the Atmospheric GCM for the Earth Simulator (AFES) and European Centre for Medium-Range Weather Forecasts (ECMWF) Integrated Forecast System (IFS). In their formulation, spherical harmonics functions are employed. The nonlinear transfer term was separated into horizontal and vertical contributions. The horizontal nonlinear transfer is conservative. As a result, the direction of the energy cascade can also be identified by this formulation. They found a strong downscale energy cascade in the mesoscale for the AFES model. However, AFES has low vertical resolution (e.g., Hamilton et al. 2008), which can affect the mesoscale spectrum (e.g., Waite 2016).

Malardel and Wedi (2016) conducted a kinetic and available potential energy spectral analysis of the IFS model. In particular, the spectral analysis techniques developed by Augier and Lindborg (2013) were used to examine the role of physical parameterizations in the k^{-3} spectrum at the synoptic scale and $k^{-5/3}$ spectrum at the mesoscale. Malardel and Wedi

(2016) found that KE and APE spectra and their spectral energy fluxes were significantly affected by physical parameterizations. For example, KE and APE spectra were smaller in adiabatic simulations than in the full physics simulations at all scales except at very large scales. The energy flux for the conversion from APE to KE was also significantly affected at different scales when the deep convection parameterization or vertical diffusion parameterization was disabled. The choice of physical parameterization could affect the energy cascade. As suggested by Malardel and Wedi (2016), if physical processes were not represented properly due to resolution and subgrid-scale parameterizations, the parameterized energy transfer would not be realistic.

Sun et al. (2017) conducted an energy spectral budget analysis of an idealized nonhydrostatic mesoscale convective system simulation. The $k^{-5/3}$ spectrum was found from the lower troposphere to the lower stratosphere. At small scales, buoyancy flux injected kinetic energy in the upper troposphere and the vertical flux divergence distributed energy in the vertical directions through convection and inertia gravity waves. Such results suggested that the mechanisms responsible for the spectrum could be three-dimensional. In other words, an inverse cascade was unlikely to be the main responsible mechanism in mesoscale convective systems. However, the simulations were short and far from equilibrium, and there were no surface fluxes. As a result, it is not clear how relevant this is to RCE over longer time scales.

We investigate the mechanisms and energy cascade in RCE simulations with and without self-aggregation by performing an analysis of the atmospheric energy spectrum and the spectral energy budget. By analyzing the spectral budget and comparing nonaggregated and aggregated simulations, we can understand the role of convection on the development of the kinetic energy spectrum and the spectral energy budget. The rest of this paper is organized as follows. In section 2, we present the methodology and the details of the spectral budget. Results and discussion are presented in section 3. In section 3a, an overview of the simulation is presented. In section 3b, we discuss kinetic energy spectra and spectral budget. In section 3c, we discuss nonlinear spectral energy flux. In section 3d, we discuss compensated kinetic energy spectra. In section 3e, we discuss the effect of rotation on kinetic energy spectra and spectral budget. Conclusions are given in section 4. The details on numerical dissipation are given in the appendix.

2. Methodology

a. Model

We use the Advanced Research Weather Research and Forecasting (WRF) Model to perform all simulations (Skamarock et al. 2008). The fully compressible nonhydrostatic Euler equations are solved in WRF (Skamarock et al. 2008) with a third-order Runge–Kutta time-stepping scheme, a third-order advection scheme in the vertical, and a fifth-order advection scheme in the horizontal. Terrain-following hydrostatic pressure is used as the vertical coordinate.

The setup of our simulations is modified from the radiative–convective equilibrium test case from WRF. The initial temperature and moisture profiles are from Rotunno and Emanuel (1987). The domain size is $L(x) \times L(y) \times H(z)$, where $L = 600$ km and $H = 25$ km. The horizontal grid spacing is $\Delta x = 4$ km, with 199 grid levels in the vertical. The vertical level spacing is about 100 m from the ground to 15 km, above which the vertical resolution stretches to a level spacing of about 400 m at the top of the domain. Simulations are run for 77 days. Boundary conditions are periodic in x and y. In the top 5 km of the domain, Rayleigh damping with a damping coefficient of 0.003 s^{-1} is applied. There is no rotation, except for in one rotation test case, or imposed background wind.

A brief overview of parameterizations used will be given here. No planetary boundary layer (PBL) scheme is used. The SST is set to 302 K. Other RCE studies have performed simulations with similar SST (e.g., Colin et al. 2019; Tompkins and Semie 2017). Revised MM5 Monin–Obukhov surface layer scheme (Jiménez et al. 2012), and RRTMG radiation scheme for longwave and shortwave radiation are used. There is no diurnal cycle and the incoming solar radiation is set to 434.12 W m^{-2}, which corresponds to an effective zenith angle of 50.5° (e.g., Holloway and Woolnough 2016). We use the Thompson microphysics scheme (Thompson et al. 2008). The subgrid turbulence mixing scheme used in simulations presented is the 1.5-order TKE closure model (Skamarock et al. 2008).

b. Kinetic energy spectrum and spectral budget

The horizontal kinetic energy (HKE) per unit volume contributed by horizontal wave vector $\mathbf{k} = (k_x, k_y)$ at height z is

$$E_h(\mathbf{k}, z) = \frac{1}{2}\overline{\rho}(z)[\hat{u}(\mathbf{k},z)^*\hat{u}(\mathbf{k}, z) + \hat{v}(\mathbf{k},z)^*\hat{v}(\mathbf{k}, z)], \quad (1)$$

where a hat represents Fourier coefficient and an asterisk denotes the complex conjugate. It is common to decompose the HKE into the horizontal rotational (RKE) and divergent kinetic energy (DKE) (e.g., Augier and Lindborg 2013; Waite and Snyder 2013). The horizontal kinetic energy is decomposed by Helmholtz decomposition:

$$E_h(\mathbf{k}, z) = \text{RKE}(\mathbf{k}, z) + \text{DKE}(\mathbf{k}, z), \quad (2)$$

$$\text{RKE}(\mathbf{k}, z) = \frac{1}{2}\overline{\rho}(z)\frac{\hat{\delta}^*\hat{\delta}}{k_h^2}, \quad (3)$$

$$\text{DKE}(\mathbf{k}, z) = \frac{1}{2}\overline{\rho}(z)\frac{\hat{\xi}^*\hat{\xi}}{k_h^2}, \quad (4)$$

where $k_h = |\mathbf{k}|$, and

$$\xi = \frac{\partial u}{\partial x} + \frac{\partial v}{\partial y},$$

$$\delta = \frac{\partial v}{\partial x} - \frac{\partial u}{\partial y}.$$

are the horizontal divergence and vertical vorticity of the horizontal velocity, respectively. RKE is often used to diagnose horizontal vortices, while DKE can identify energy from IGWs. DKE is significantly larger than RKE in the lower stratosphere, suggesting IGWs are important. In addition, RKE $\gtrsim$ DKE in the upper troposphere in many studies (e.g., Waite and Snyder 2013; Peng et al. 2015b).

While WRF is a compressible model, acoustic modes are damped by the semi-implicit time stepping, and so the anelastic approximation is used in the spectral budget analysis (as in, e.g., Sun et al. 2017). The anelastic approximation is often employed to simplify the governing equations in the atmosphere due to the fact that density changes with height are more significant than the changes in the horizontal (e.g., Vallis 2006). The anelastic approximation assumes that the density (ρ), pressure (p), and potential temperature (θ) can be written as the sum of a hydrostatically balanced state, which is a function of height ($\tilde{\cdot}$), and a small perturbed state ($\cdot$)′:

$$\rho = \tilde{\rho}(z) + \rho'(x, y, z, t), \tag{5}$$

$$p = \tilde{p}(z) + p'(x, y, z, t), \tag{6}$$

$$\theta = \tilde{\theta}(z) + \theta'(x, y, z, t). \tag{7}$$

In the atmosphere, the variation of density, pressure, and potential temperature at a certain height is often small compared to the balanced state (e.g., Vallis 2006), which is given by $|\rho'| \ll \tilde{\rho}(z)$. In this approximation, the continuity equation (e.g., Vallis 2006) takes the simpler form

$$\boldsymbol{\nabla} \cdot (\tilde{\rho}\,\mathbf{v}) = 0. \tag{8}$$

With the anelastic approximation, the momentum equations are written as

$$\frac{D\mathbf{v}}{Dt} = \hat{\mathbf{k}}g\theta'_v\tilde{\theta} - c_p\theta_v\boldsymbol{\nabla}\pi' + \frac{\partial\tau_{ij}}{\partial x_j}, \tag{9}$$

where $\mathbf{v} = (u, v, w) = (u_1, u_2, u_3)$ is the velocity vector in three dimension, $\boldsymbol{\nabla}$ is the three-dimensional gradient operator, θ is the potential temperature, θ_v is the virtual potential temperature, π is the Exner function (e.g., Sun et al. 2017), and τ_{ij} is the subgrid-scale stress tensor, which is a viscosity-like term for subgrid turbulence mixing modeling.

To understand the evolution of $E_h(\mathbf{k}, z)$, it is useful to consider its budget. This budget was developed by Augier and Lindborg (2013) on a spherical hydrostatic model, and modified by Peng et al. (2015a) and Sun et al. (2017) to a nonhydrostatic model with rectangular coordinates. The budget is derived by taking the Fourier transform of the momentum equations and dotting with the conjugate of the horizontal velocity vectors:

$$\frac{\partial E_h}{\partial t}(\mathbf{k}, z) = \mathrm{Re}[A(\mathbf{k}, z) + P(\mathbf{k}, z) + D(\mathbf{k}, z)], \tag{10}$$

where

$$A(\mathbf{k}, z) = -\overline{\rho}(z)\hat{u}_i^*\mathcal{F}\left(u_j\frac{\partial}{\partial x_j}u_i\right), \tag{11}$$

$$P(\mathbf{k}, z) = -\overline{\rho}(z)\hat{u}_i^*\mathcal{F}\left(c_p\theta_v\frac{\partial}{\partial x_i}\pi'\right), \tag{12}$$

$$D(\mathbf{k}, z) = \overline{\rho}(z)\hat{u}_i^*\mathcal{F}\left[\frac{\partial}{\partial x_j}(\tau_{ij})\right], \tag{13}$$

where $\mathcal{F}(\cdot)$ represents the two-dimensional horizontal Fourier coefficient of $(\cdot)$ which is dependent on z, $A(\mathbf{k}, z)$ is the energy tendency from the nonlinear advection, $P(\mathbf{k}, z)$ is the energy tendency from the pressure term, and $D(\mathbf{k}, z)$ is the energy dissipation from subgrid turbulence mixing. Note that in some other studies, the dissipation is often ignored or calculated as a residual (e.g., Peng et al. 2015a). We calculate the effect of the dissipation explicitly in our study. In the analysis of the model energy spectrum, wavelengths less than $6\Delta x$ are often ignored due to the effect of the dissipation (e.g., Bryan et al. 2003). In global or regional climate simulations, $6\Delta x$ can be the length of a convective plume or even a convective system (e.g., Bryan et al. 2003; Bryan and Morrison 2012). Dissipation is Δx dependent and purely dissipative in eddy viscosity models. Because of the importance of dissipation, we calculate the dissipative term in the spectral budget explicitly.

The advective contribution to the spectral budget $A(\mathbf{k}, z)$ can be further broken down into the contribution from the conservative horizontal nonlinear transfer $T(\mathbf{k}, z)$, which corresponds to conservative transfers of energy between different scales at the same height, the sum over $\mathbf{k}$ of which at each height is zero; and a contribution to the divergence of vertical energy flux (e.g., Augier and Lindborg 2013; Peng et al. 2015a; Sun et al. 2017):

$$A(\mathbf{k}, z) = -\overline{\rho}\hat{\mathbf{u}}^*\cdot\mathcal{F}\left(\mathbf{u}\cdot\nabla_h\mathbf{u} + \mathbf{u}\frac{\nabla_h\cdot\mathbf{u}}{2}\right) \tag{14}$$

$$-\frac{1}{2}\overline{\rho}\hat{\mathbf{u}}^*\cdot\mathcal{F}\left(w\frac{\partial\mathbf{u}}{\partial z}\right) + \frac{1}{2}\overline{\rho}\frac{\partial\hat{\mathbf{u}}^*}{\partial z}\cdot\mathcal{F}(w\mathbf{u}) \tag{15}$$

$$-\frac{1}{2}\frac{\partial[\overline{\rho}\hat{\mathbf{u}}^*\cdot\mathcal{F}(w\mathbf{u})]}{\partial z}, \tag{16}$$

$$= T(\mathbf{k}, z) - \frac{1}{2}\frac{\partial[\overline{\rho}\hat{\mathbf{u}}^*\cdot\mathcal{F}(w\mathbf{u})]}{\partial z}, \tag{17}$$

where (14) and (15) can be defined as the horizontal nonlinear transfer $T(\mathbf{k}, z)$ and (16) is a part of the divergence of vertical energy flux and it is defined as

$$V_{\mathrm{adv}}(\mathbf{k}, z) = -\frac{1}{2}\frac{\partial[\overline{\rho}\hat{\mathbf{u}}^*\cdot\mathcal{F}(w\mathbf{u})]}{\partial z}.$$

The pressure term $P(\mathbf{k}, z)$ can be decomposed into a contribution from the buoyancy flux and another contribution to the divergence of vertical energy flux (e.g., Augier and Lindborg 2013; Peng et al. 2015b; Sun et al. 2017):

$$P(\mathbf{k}, z) \approx -c_p \frac{\partial}{\partial z}(\overline{\rho}\overline{\theta}\hat{w}^*\hat{\pi}') \tag{18}$$

$$+ c_p\overline{\rho}\overline{\theta}\hat{w}^*\mathcal{F}\left(\frac{\partial\pi'}{\partial z}\right), \tag{19}$$

$$= -c_p \frac{\partial}{\partial z}(\overline{\rho}\overline{\theta}\hat{w}^*\hat{\pi}') + B(\mathbf{k}, z), \tag{20}$$

where (19) is the buoyancy flux $B(\mathbf{k}, z)$. The vertical flux from (16) and (18) are collected to form the divergence of vertical energy flux $V(\mathbf{k}, z)$, which is given below.

In summary,

$$\frac{\partial E}{\partial t}(\mathbf{k}, z) = \text{Re}[T(\mathbf{k}, z) + B(\mathbf{k}, z) + V(\mathbf{k}, z) + D(\mathbf{k}, z)], \tag{21}$$

where

$$T(\mathbf{k}, z) = -\overline{\rho}\hat{\mathbf{u}}^* \cdot \mathcal{F}\left(\mathbf{u} \cdot \nabla_h\mathbf{u} + \mathbf{u}\frac{\nabla_h \cdot \mathbf{u}}{2}\right) \tag{22}$$

$$- \frac{1}{2}\overline{\rho}\hat{\mathbf{u}}^* \cdot \mathcal{F}\left(w\frac{\partial\mathbf{u}}{\partial z}\right) + \frac{1}{2}\overline{\rho}\frac{\hat{\partial\hat{\mathbf{u}}}^*}{\partial z} \cdot \mathcal{F}(w\mathbf{u}), \tag{23}$$

$$B(\mathbf{k}, z) = c_p\overline{\rho}\overline{\theta}\hat{w}^*\mathcal{F}\left(\frac{\partial\pi'}{\partial z}\right), \tag{24}$$

$$V(\mathbf{k}, z) = -\frac{1}{2}\frac{\partial[\overline{\rho}\hat{\mathbf{u}}^* \cdot \mathcal{F}(w\mathbf{u})]}{\partial z} - c_p\frac{\partial}{\partial z}(\overline{\rho}\overline{\theta}\hat{w}^*\hat{\pi}'), \tag{25}$$

$$D(\mathbf{k}, z) = \overline{\rho}\hat{u}_i^*\mathcal{F}\left(\frac{\partial}{\partial x_j}\tau_{ij}\right). \tag{26}$$

Due to computational limitations, it is not possible to resolve the smallest eddies directly. As a result, Smagorinsky (1963) suggested the eddy viscosity model which parameterizes the subgrid eddies with a viscosity-like term. The subgrid stress tensor τ_{ij} is defined as

$$\tau_{ij} = K_{h,v}D_{ij}, \tag{27}$$

where D_{ij} is the deformation tensor, with $i, j = 1, 2, 3$, K_h is the eddy viscosity for $i, j = 1, 2$, and K_v is the eddy viscosity for i or $j = 3$. In the TKE closure model, K is computed using the evolution of the subgrid turbulence kinetic energy:

$$K_{h,v} = C_k e^{1/2}\Delta_{h,v}, \tag{28}$$

where C_k is a constant, Δ_h is the horizontal grid spacing, and Δ_v is the vertical grid spacing; e is the subgrid turbulence kinetic energy and its evolution is predicted with a model equation (e.g., Wyngaard 2010).

In this study, we will also consider the effect of numerical dissipation. WRF uses a third-order upwind advection scheme in the vertical, and a fifth-order upwind advection scheme in the horizontal (Skamarock et al. 2008), both of which have weak dissipation. The calculation of the numerical dissipation is described in the appendix.

All two-dimensional energy and budget spectra on the k_x–k_y plane are transformed to one-dimensional spectra on k_h as in Waite and Snyder (2009):

$$E(k_h)\Delta k = \sum_{k_h-0.5\Delta k \le |\mathbf{k}| \le k_h+0.5\Delta k} E(\mathbf{k}), \tag{29}$$

where k_h is the nondimensionalized horizontal wavenumber, $\Delta k = 2\pi/L$ is the wavenumber spacing, and similarly for spectra of $T(k_h, z)$, $B(k_h, z)$, $V(k_h, z)$, and $D(k_h, z)$. Unless otherwise specified, $D(k_h, z)$ includes both eddy dissipation and numerical dissipation.

The nonlinear spectral energy flux $\Pi(k_h, z)$ is defined as (e.g., Peng et al. 2015b)

$$\Pi(k_h, z) = \Delta k \sum_{k \ge k_h} \text{Re}[T(k, z)], \tag{30}$$

where $\Delta k = 2\pi/L$; $\Pi(k_h, z)$ is the rate at which kinetic energy is transferred downscale past wavenumber k_h at height z. Positive Π implies forward energy transfer and negative Π suggests inverse energy transfer. A downscale cascade is characterized by a wide range of constant positive $\Pi(k_h, z)$.

When computing energy spectra and the energy spectral budget terms, fields are interpolated from WRF Model levels to a constant height at every 50 m, which is about half of the vertical resolution of the simulation from the lower troposphere to the lower stratosphere (as in Sun et al. 2017). Nonlinear terms are computed after interpolating to higher horizontal resolution to eliminate aliasing (e.g., Durran 2010). This approach ensures that $T(\mathbf{k}, z)$ is indeed conservative. Horizontal derivatives are computed with Fourier transform and the vertical derivatives are computed with the second-order central finite difference scheme. All energy spectra presented are averaged in both time (final 42 days of simulation) and height. In the following discussion, the upper troposphere is defined as the region between 6 and 10 km in height and the lower stratosphere is defined as the region between 15.5 and 17 km in height.

Two main simulations will be discussed: one with and one without aggregation. Unless otherwise specified, we will focus our following discussion on the two simulations without rotation. Note that whether or not aggregation occurs is strongly affected by the subgrid turbulence scheme. It is very hard to get aggregation if the standard TKE subgrid turbulence scheme is used. Inspired by Tompkins and Semie (2017), we have multiplied the TKE coefficient (C_k) by two in the aggregated simulation. In the following discussion, we will call the simulation with the default TKE coefficient ($C_k = 0.15$) the nonaggregated simulation and the simulation the larger TKE coefficient ($C_k = 0.3$) the aggregated simulation. The configuration of the nonaggregated and aggregated simulations are otherwise identical. We will discuss the evolution, horizontal kinetic energy spectra, and the spectral budgets of the aggregated and nonaggregated simulations in this section. Note that features with length scale of less than $6\Delta x$ ($k_h > 25$) are often considered as not well-resolved (e.g., Sun et al. 2017; Menchaca and Durran 2019). As a result, findings from scales smaller than $6\Delta x$ (24 km) will be interpreted with care.

Not surprisingly, we find that the energy budget at these marginally resolved scales is dominated by dissipation. An additional shorter simulation with rotation added will be presented to briefly demonstrate the effect of rotation on the kinetic energy spectrum and the spectral energy budget. The detail of the rotation simulation will be given in the corresponding subsection.

3. Results and discussion

a. Overview of the simulations

To identify and quantify aggregation, we visualize the evolution of the outgoing longwave radiation at top of the atmosphere (TOA OLR) in Fig. 1. In the nonaggregated simulation (Figs. 1a–h), the system reaches approximate equilibrium at about 320 h. After the simulation reaches equilibrium, the convective cores are randomly distributed over the whole domain and remain so throughout the remaining time of the nonaggregated simulation (Figs. 1a–h). Note that the convective system develops some large-scale structure at late times (e.g., Figs. 1e–h), but they are very different from the large isolated convective structure that develops in the aggregated case. In the aggregated simulation (Figs. 1i–p), the convective cores are randomly distributed in the domain at early times. The convective cores aggregate significantly after 160 h and the simulation reaches an aggregated state, with one large cloud region surrounded by a dry region, after about 480 h (Figs. 1k–p).

We find that aggregation changes mean profiles, which agrees with findings from other studies (e.g., Wing et al. 2017). In the nonaggregated simulation, there are no significant changes to the water vapor mixing ratio profile throughout the simulation (Fig. 2a). In contrast, the lower troposphere in the aggregated simulation dries as the convective system reaches an aggregated state (Fig. 3a). The drying in the troposphere in the aggregated simulation has also been reported in other studies (e.g., Bretherton et al. 2005; Wing and Cronin 2016). The vertical profile of the cloud water plus cloud ice mixing ratio changes throughout the simulation for nonaggregated simulation (Fig. 2b). On the other hand, there is a significant increase in cloud condensate (cloud water plus cloud ice) over time in the lower troposphere of the aggregated simulation (Fig. 3b), which is consistent with the findings from other studies such as Wing and Cronin (2016). Note that while Wing and Cronin (2016) found that there was a reduction in cloud condensate in the midtroposphere with aggregation, there is no obvious trend of increase or decrease in midtroposphere liquid condensate in our study. The cloud-top height of the aggregated simulation is slightly lower than the cloud-top height of the nonaggregated simulation (Figs. 2b and 3b).

The variance of frozen moist static energy (e.g., Wing and Emanuel 2014; Wing et al. 2017) or OLR (e.g., Muller and Held 2012) can be employed to quantify aggregation. We will use the variance of frozen moist static energy to quantify aggregation. As we can see in Figs. 2d and 3d, the variance of FMSE in the aggregated simulation is significantly larger than the variance in the nonaggregated simulation. A larger variance of FMSE suggests the convective system is more

aggregated in line with the findings above. According to the variance of FMSE time series, the nonaggregated simulation reaches a stable state at about 300 h (Fig. 2d) as found above. After that, we can see that the variance of FMSE oscillates around the same level throughout the remaining simulation time and increases slightly at around 800 h. After it reaches the peak at about 950 h, it drops significantly from 950 to 1600 h. The fact that the variance of FMSE oscillates from 300 to 800 h suggests that the convective system aggregates and disaggregates slightly even after it reaches its equilibrium state. Similarly, the convective system in the aggregated simulation reaches its most aggregated state at about 450 h, then it disaggregates slightly. After the drop at 450 h, the variance of the FMSE oscillates. The oscillation in variance of FMSE suggests that the convective system in the aggregated also aggregates and disaggregates throughout the simulation. Overall, while there are some significant variations in the FMSE time series in Fig. 2d, the overall magnitude of the FMSE variance is still much smaller than in the aggregated case in Fig. 3d. The different OLR structures in Fig. 1, and the different FMSE variance magnitudes in Figs. 2 and 3, support the identification of these cases as nonaggregated and aggregated.

b. Kinetic energy spectra and budget

In this section, we will discuss the difference in the horizontal kinetic energy spectrum and spectral budget of the aggregated and nonaggregated simulation in the upper troposphere. After that, we will discuss the difference in the lower stratosphere.

1) Upper troposphere

The horizontal kinetic energy spectrum for the nonaggregated simulation in the upper troposphere is much shallower than the $-5/3$ spectrum (Fig. 4a). By contrast, the horizontal kinetic energy spectrum for the aggregated simulation in the upper troposphere is steeper than the nonaggregated case and closer to $-5/3$ (Fig. 4b). The fact that the horizontal kinetic energy spectrum is more energetic at scales of $O(100)$ km in the aggregated simulation is consistent with the size of the aggregated convective cores (Fig. 1). The convective core in the aggregated simulation aggregates and forms a large convective system of a few hundred kilometers in size, which is not seen in the nonaggregated simulation.

Horizontal kinetic energy equals the sum of divergent kinetic energy and rotational kinetic energy. In the nonaggregated simulation, RKE is similar to DKE over most scales in the upper troposphere, with the DKE spectrum marginally larger than the RKE spectrum for $k_h < 40$ (Fig. 4a). In the aggregated simulation, the DKE $\gtrsim$ RKE for $k_h < 30$ (Fig. 4b). In other studies such as Waite and Snyder (2013) and Peng et al. (2015b), it was found that RKE $\gtrsim$ DKE in the upper troposphere, while DKE dominates in our simulations. The difference is likely due to the fact that their simulations were driven by large-scale vortices and rotation, while our nonaggregated and aggregated simulations are driven by surface fluxes and convection in a nonrotating environment. This conclusion is confirmed by the rotation simulation presented in section 3e.
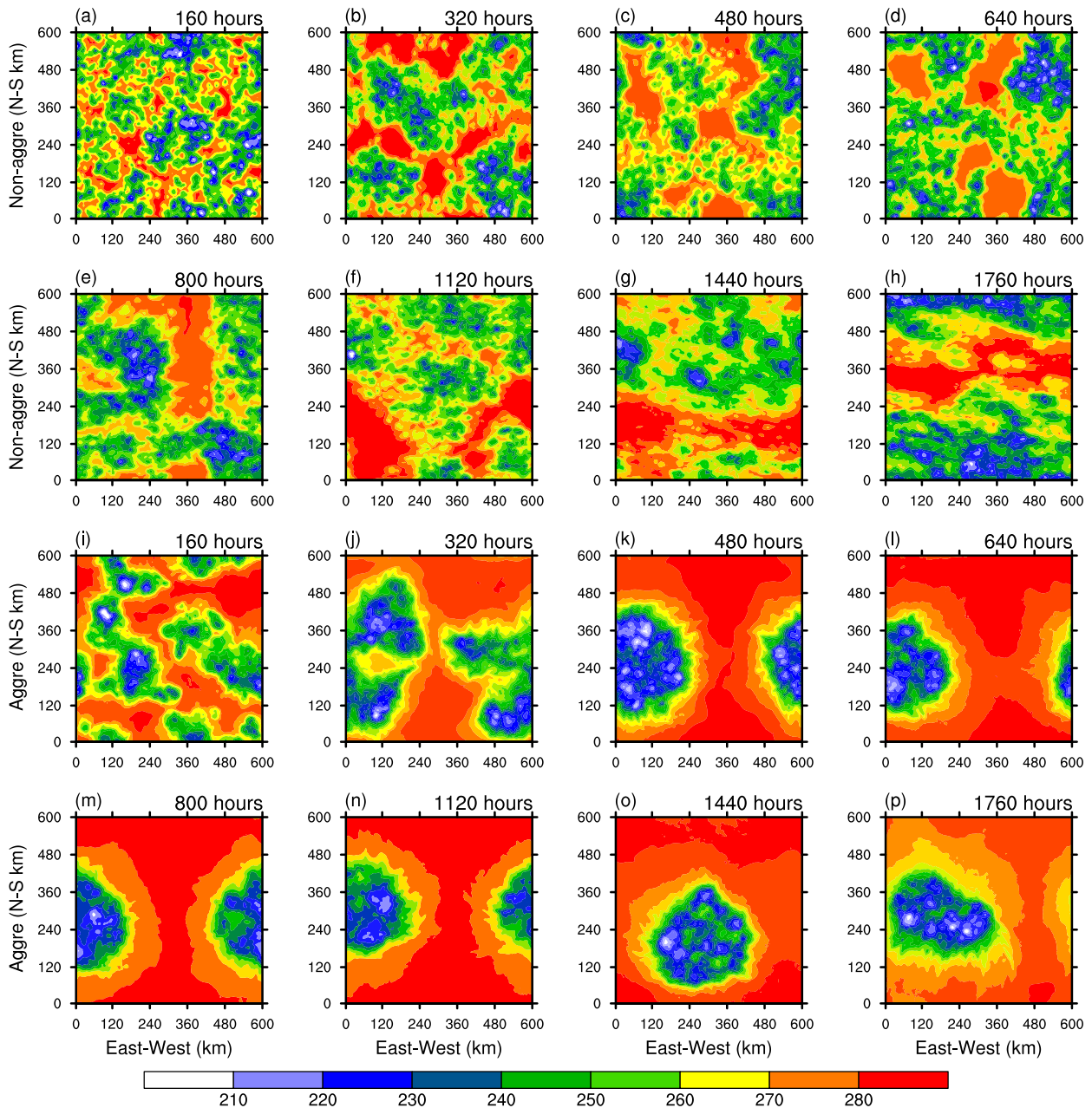
TOA OLR

FIG. 1. The outgoing longwave radiation (W m^{-2}) at top of the atmosphere (TOA OLR) for the nonaggregated simulation at $t =$ (a) 160, (b) 320, (c) 480, (d) 640, (e) 800, (f) 1120, (g) 1440, and (h) 1760 h and for the aggregated simulation at $t =$ (i) 160, (j) 320, (k) 480, (l) 640, (m) 800, (n) 1120, (o) 1440, and (p) 1760 h.

The tendency of the horizontal kinetic energy spectrum can be decomposed into the nonlinear transfer $T(k_h)$, the vertical energy flux $V(k_h)$, the buoyancy flux $B(k_h)$, and the dissipation $D(k_h)$. In the upper troposphere, the nonaggregated simulation gains kinetic energy from the buoyancy flux term and loses energy from vertical energy flux and dissipation (Fig. 4c). The energy gain from the buoyancy flux and energy

loss from the vertical energy flux is approximately balanced for $k_h < 30$ (wavelengths larger than 20 km). Moist processes energize the mesoscale by directly injecting energy at the mesoscale (as in Waite and Snyder 2013). Convection adds latent heating and potential energy, some of which is converted to KE by the buoyancy flux. Hence, the buoyancy flux injects kinetic energy to the flow. Most of this kinetic energy is
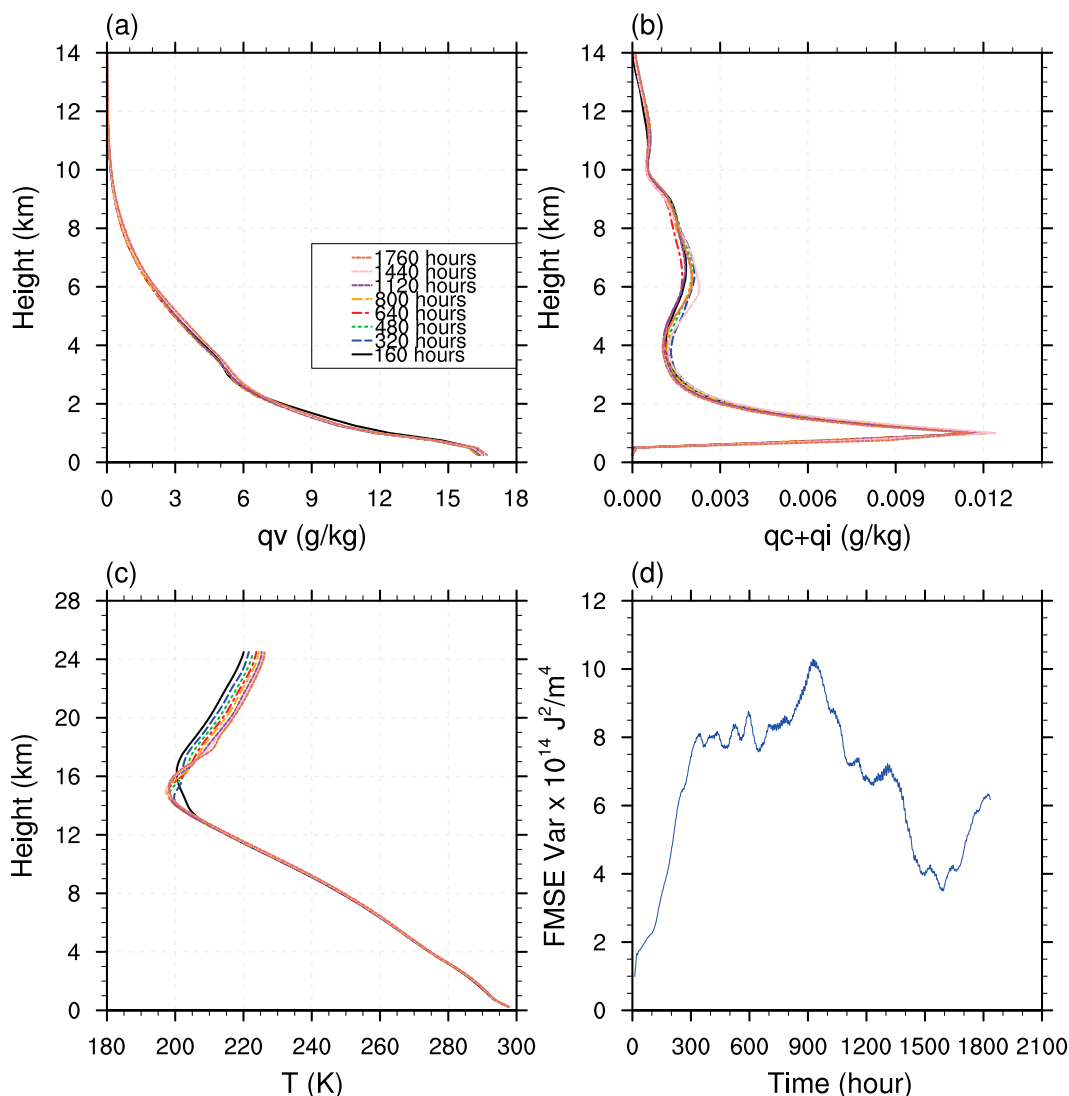
FIG. 2. Vertical profiles of (a) water vapor mixing ratio, (b) cloud water plus cloud ice mixing ratio, and (c) temperature at $t = 160$ (black), 320 (blue), 480 (green), 640 (red), 800 (orange), 1120 (purple), 1440 (light pink), and 1760 h (dark pink) and (d) the time series of the variance of vertically integrated frozen moist static energy (FMSE) for the nonaggregated simulation. The variance of vertically integrated FMSE is smoothed with a 24-h moving average.

removed from the upper troposphere by vertical energy fluxes. The energy loss from the vertical energy flux is likely associated with the upward-propagating gravity waves. At smaller scales, the energy gain from buoyancy flux is mainly balanced by the loss of energy from dissipation at $k_h > 30$, which corresponds to wavelength of 20 km or less. The energy gain from buoyancy flux and the energy loss from dissipation both peak at about $k_h = 75$, which corresponds to a wavelength of $2\Delta x$. Recall that scales smaller than $6\Delta x$, or $k_h < 25$, are only marginally resolved. Kinetic energy from buoyancy flux is mainly generated at the smallest scales in the nonaggregated simulation. At all scales, the nonlinear transfer term is weak compared to the other terms in the budget. Note that the transfer term is conservative, so the sum of the transfer term should be zero. We can see that there is a positive

contribution for the transfer term for $k_h > 20$, which suggests that there is a negative contribution from $k_h < 20$. This means energy transfer from large scale to small scales, which corresponds to downscale energy transfer.

The terms in the spectral budget for the aggregated simulation in the upper troposphere are weaker than the terms for the nonaggregated simulation (Fig. 4d). Unlike the nonaggregated simulation, the energy gain from the buoyancy flux is not mainly balanced by the loss of energy from the vertical energy flux for $k_h < 3$ in the aggregated simulation; rather, it is balanced by the loss of energy from the transfer term and the vertical energy flux. Note that $k_h < 3$ corresponds to length scales larger than 200 km, which is approximately the size of the convective core in the aggregated simulation. The energy gain from the buoyancy flux is balanced by the energy
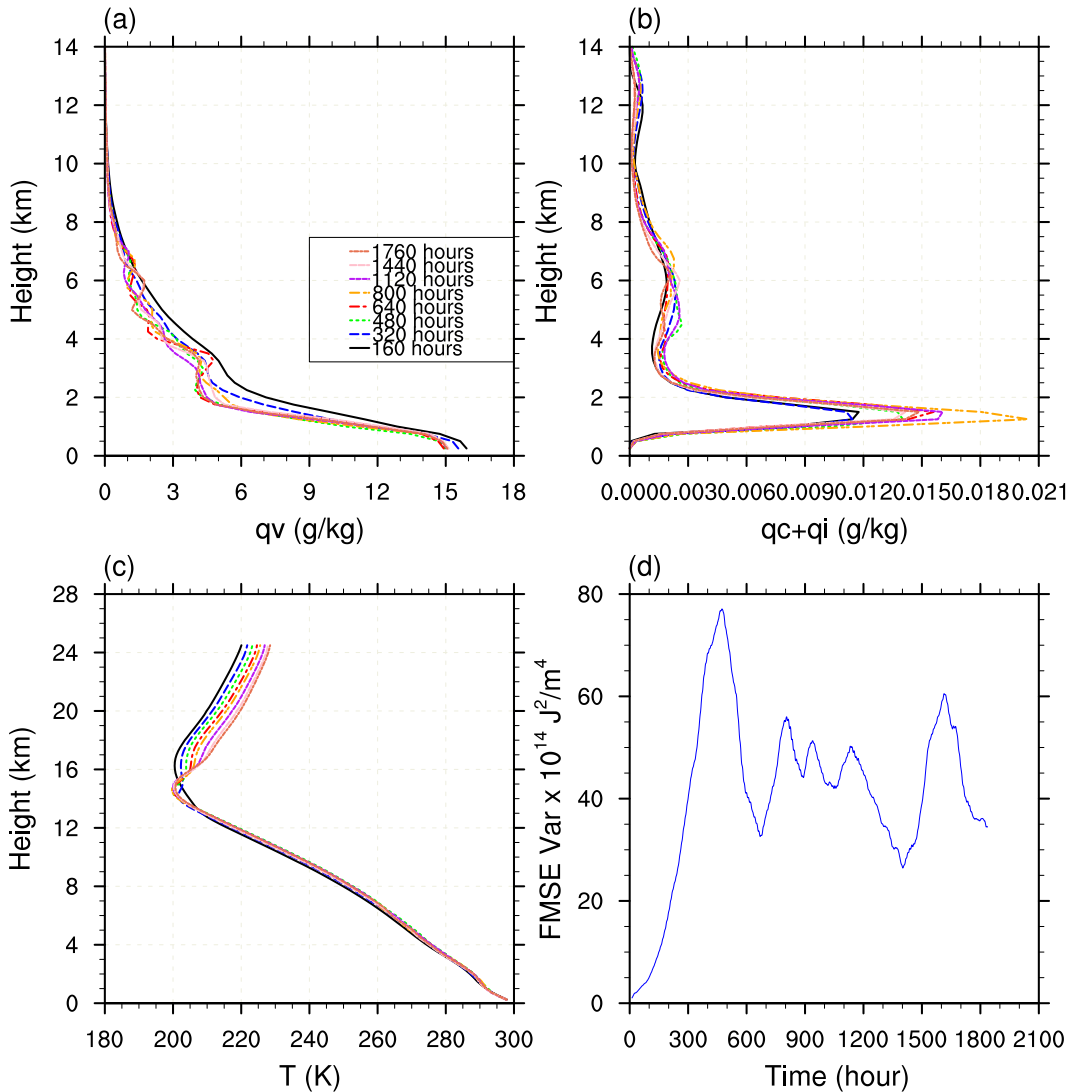
FIG. 3. As in Fig. 2, but for the aggregated simulation.

loss in the vertical energy flux at smaller scales in the aggregated simulation for $3 < k_h < 30$. For $k_h > 30$, there is energy gain from the vertical energy flux for the aggregated simulation, which is different from the nonaggregated simulation; while there is still a positive contribution from the buoyancy flux at these scales, it is not the dominant term. Note that scales smaller than $6\Delta x$ ($k_h > 25$) are not well-resolved. The positive contributions from the vertical energy flux, transfer, and buoyancy flux are balanced by the dissipation. Similar to the nonaggregated simulation, there is a positive contribution for the transfer term at large k_h, which again implies that there is downscale energy transfer. Nevertheless, since the transfer term contributes a relatively small part to the overall spectral budget, the spectrum does not appear to result from a turbulent cascade; rather, it is due to a balance between forcing by buoyancy flux and removal by vertical energy flux. The fact that the kinetic energy spectrum of the aggregated simulation is steeper than that in the nonaggregated case, and

closer to the $-5/3$ spectrum, may be due to the fact that B, which adds kinetic energy, has a much broader spectrum in the aggregated simulation than in the nonaggregated simulation, where is it more dominated by small scales. Notice that the buoyancy flux and vertical energy flux divergence terms peak at a smaller wavelength in the nonaggregated simulation than in the aggregated simulation. This is reasonable because of the convective core in the aggregated simulation corresponds to a larger wavelength than the convective core in the nonaggregated simulation. The fact that there is a change in sign in the vertical energy flux term at small scales in the upper troposphere for the aggregated simulation (Fig. 4d) is different from what was found in Sun et al. (2017), in which buoyancy flux was positive and vertical energy flux was negative in the upper troposphere at all wavelength. Note that the peak of all the terms in the spectral budget in the upper troposphere are at $k_h = 75$ for both simulations, which suggests that, as expected, $\Delta x = 4$ km may not be sufficient to fully resolve small-scale convection.
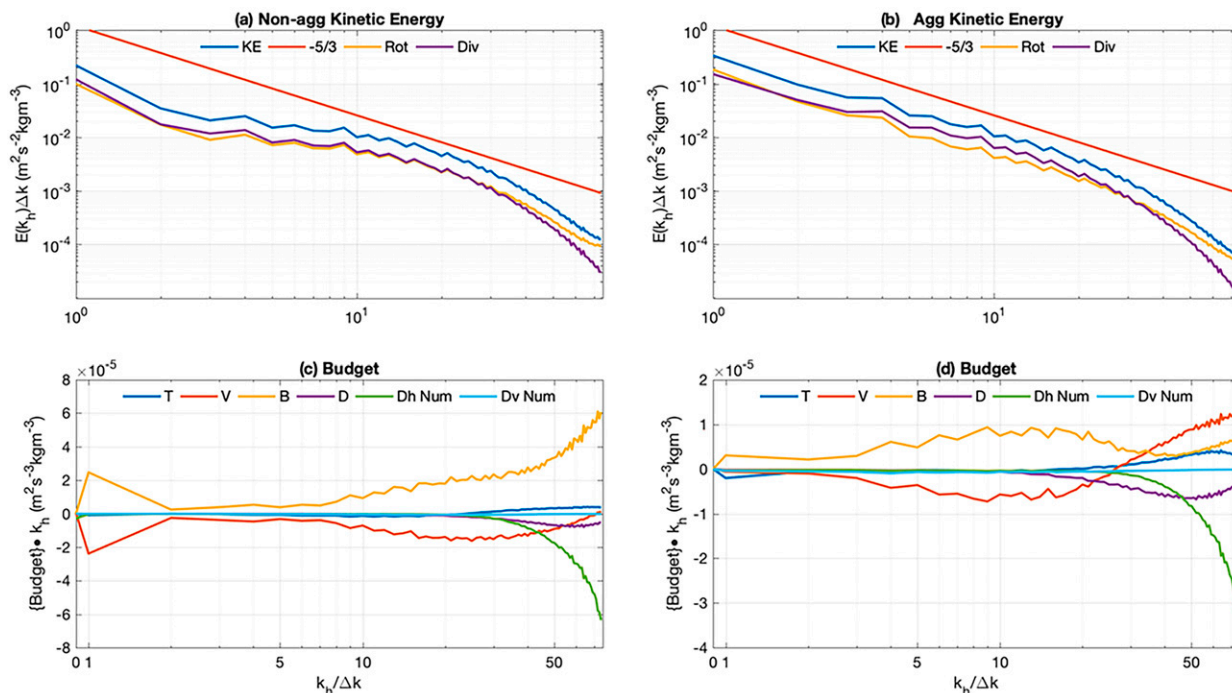
FIG. 4. The horizontal kinetic energy spectrum (blue), rotational kinetic energy spectrum (yellow), and divergent kinetic energy spectrum (purple) in the upper troposphere (6–10 km) for (a) the nonaggregated simulation and (b) the aggregated simulation; and the spectral budget, including horizontal nonlinear energy transfer (blue), buoyancy flux (yellow), vertical energy flux divergence (red), dissipation from the subgrid mixing scheme (purple), and numerical dissipation (green), in the upper troposphere for (c) the nonaggregated simulation and (d) aggregated simulation. All spectra are averaged in the vertical and in time from 841 to 1848 h. Budget spectra are multiplied by k_h, for all k_h except for $k_h = 0$, to preserve area on semilog plots. Note that $k_h = 0$ is shown in (c) and (d).

Figures 5a and 5c show the sum of the computed budget terms along with the tendency of the horizontal kinetic energy spectrum. The budget is approximately balanced for the well-resolved wavenumbers $k_h < 25$ in both the aggregated and nonaggregated. Note that features with length scale of less than $6\Delta x$ ($k_h > 25$) are often considered as not well-resolved and we should treat the result in the underresolved range with care. Even at large k_h, the residual is less than 13% of the maximum terms in the budget, and is likely due to additional model damping terms and error.

2) LOWER STRATOSPHERE

In the lower stratosphere, the nonaggregated horizontal kinetic energy spectrum is again shallower than $-5/3$ (Fig. 6a). The horizontal kinetic energy spectrum for the nonaggregated simulation is less energetic than the spectrum from the aggregated simulation (Fig. 6b), which resembles the $-5/3$ spectrum for $4 < k < 20$ (wavelength between 30 and 150 km). The divergent kinetic energy dominates the horizontal kinetic energy at all wavenumbers in both the nonaggregated and aggregated simulations, as reported in other studies (e.g., Menchaca and Durran 2019). In Menchaca and Durran (2019), their Fig. 6b, we can see that the DKE dominated the horizontal kinetic energy spectrum from wavelength of 60 to 180 km and the RKE dominated the horizontal kinetic energy spectrum in the larger scales. The domination of the DKE in all wavelength in our

study is likely due to the fact that there is no rotation in our nonaggregated and aggregated simulations, which is confirmed by the simulation with rotation (see section 3e). Both the horizontal kinetic energy spectra from the aggregated and nonaggregated steepen for $k_h > 30$. The steepening of the spectrum at wavelengths smaller than $6\Delta x$ has also been found in other studies (e.g., Peng et al. 2015a; Sun et al. 2017; Menchaca and Durran 2019) and is due to numerical dissipation and the subgrid turbulence scheme.

The spectral budgets for both the aggregated and nonaggregated simulations in the lower stratosphere are similar in overall shape, but different in magnitude (Figs. 6c,d). The terms of the spectral budget from the aggregated simulation are about an order of magnitude smaller than those from the nonaggregated simulation. For both the aggregated and the nonaggregated simulation, the vertical energy flux is the main source of energy gain. The transfer and buoyancy flux removes kinetic energy at most length scales, except for the horizontal mean flow at $k_h = 0$. Similar to what was found in the upper troposphere, the aggregated simulation produces a steeper KE spectrum closer to $-5/3$ at larger scales because V, which adds kinetic energy, has a much broader than in the nonaggregated simulation, which are more dominated by smaller scales. The dissipation removes energy at a rate that is about half of the transfer term for both simulations. The energy gain from the vertical energy flux is removed by the
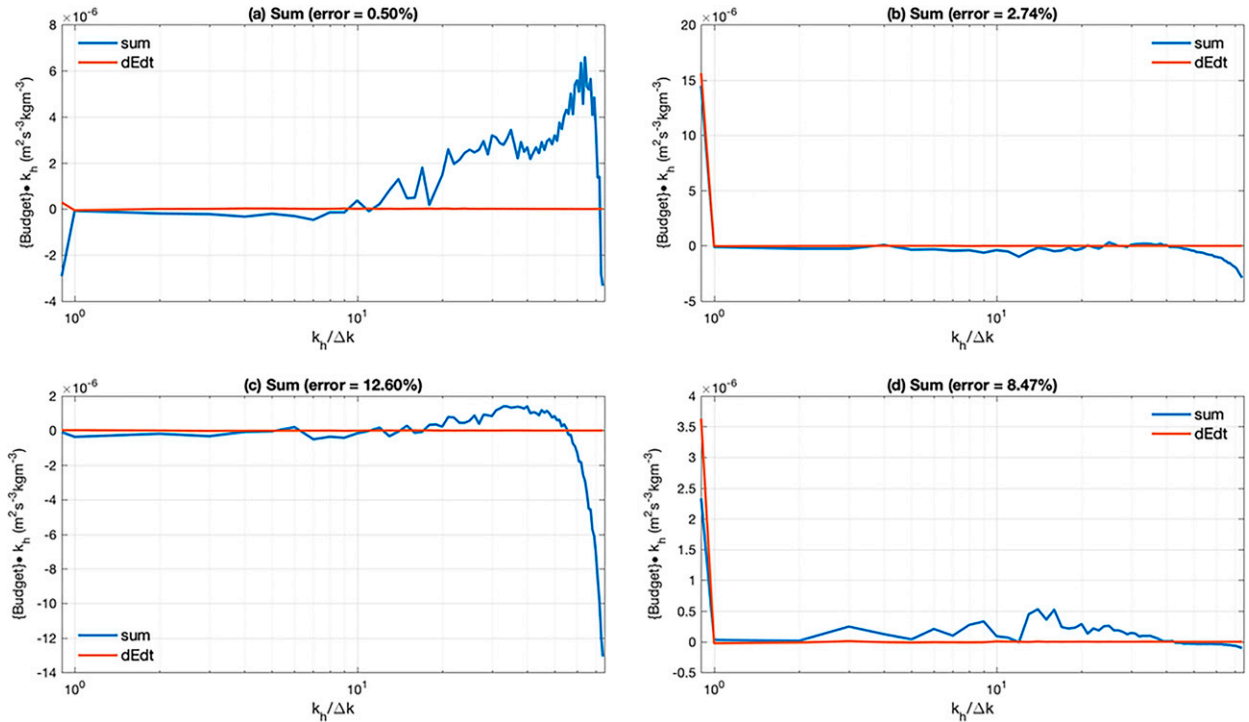
FIG. 5. The rate of change of kinetic energy spectrum (dE/dt) is compared to the sum of the budget for the nonaggregated simulation (a) in the upper troposphere and (b) in the lower stratosphere, and for the aggregated simulation (c) in the upper troposphere and (d) in the lower stratosphere. The error is the ratio between the absolute value of the difference between the sum of the budget and dE/dt and the maximum of the absolute value of all the terms in the budget.

transfer term, the buoyancy flux, and the dissipation, similar to what was found in Sun et al. (2017). Sun et al. (2017) found that a significant amount of kinetic energy was injected by the vertical energy flux in the lower stratosphere and that energy was removed by the transfer term, the buoyancy flux, and the dissipation. Also note that in Menchaca and Durran (2019), while the vertical energy flux injected energy at wavelengths from 50 to 180 km, it also removed energy at large scales of 900 km.

While the transfer term is not significant in the upper troposphere, it is more important in the lower stratosphere. Since the transfer term is conservative, the loss of energy from $k_h > 1$ means that there is an energy gain at $k_h \leq 1$. In other words, there is an upscale energy transfer in the lower stratosphere for both the aggregated and nonaggregated simulation. In particular, most of the upscale transfer goes into the mean flow ($k_h = 0$). The dissipation is removing energy at small scales in both simulations, which is consistent with other studies such as Sun et al. (2017).

The sum of all the terms in the spectral budget matches relatively well with the tendency of the horizontal kinetic energy. The difference between the sum of all the terms and the tendency is less than 9% of the maximum of all the terms for both the aggregated simulation and the nonaggregated simulation (Figs. 5b,d). Be mindful that features with $k_h > 25$ are often considered not well-resolved.

c. Nonlinear spectral energy flux

In the above discussion of the nonlinear transfer, we see that the direction of energy transfer can be determined by the shape of the transfer term. A more systematic way of determining the direction of energy transfer is to look at the nonlinear spectral energy flux. If the nonlinear spectral energy flux is positive (negative), it means that there is direct, downscale (inverse, upscale) energy transfer.

For the nonaggregated simulation, direct energy transfer or weakly inverse energy transfer can be found in the upper troposphere at all scales (Fig. 7). By contrast, at heights above 11 km, inverse energy transfer happens at almost all scales (Fig. 7) for the nonaggregated simulation, except for some direct energy transfer at heights from 14 to 15 km.

Similarly, for the aggregated simulation, we can see that at heights from 6 to 10 km (upper troposphere), there is direct energy transfer at $k_h > 2$ (Fig. 8). At a height above 12.5 km, inverse energy transfer dominates at $k_h = 2$–30 (Fig. 8). A direct energy cascade has also been reported in Augier and Lindborg (2013) and Peng et al. (2015b). Peng et al. (2015b) found that there was a direct energy cascade for scale less than 2000 km in a baroclinic wave in the upper troposphere.

Note that the sum of $T(k_h)$ has to be zero. The fact that we see $T(k_h > 0) < 0$ at most scales in the lower stratosphere for both simulations suggests that $T(0)$ has to be larger than zero, which is also confirmed by the budgets in Fig. 6. In fact,
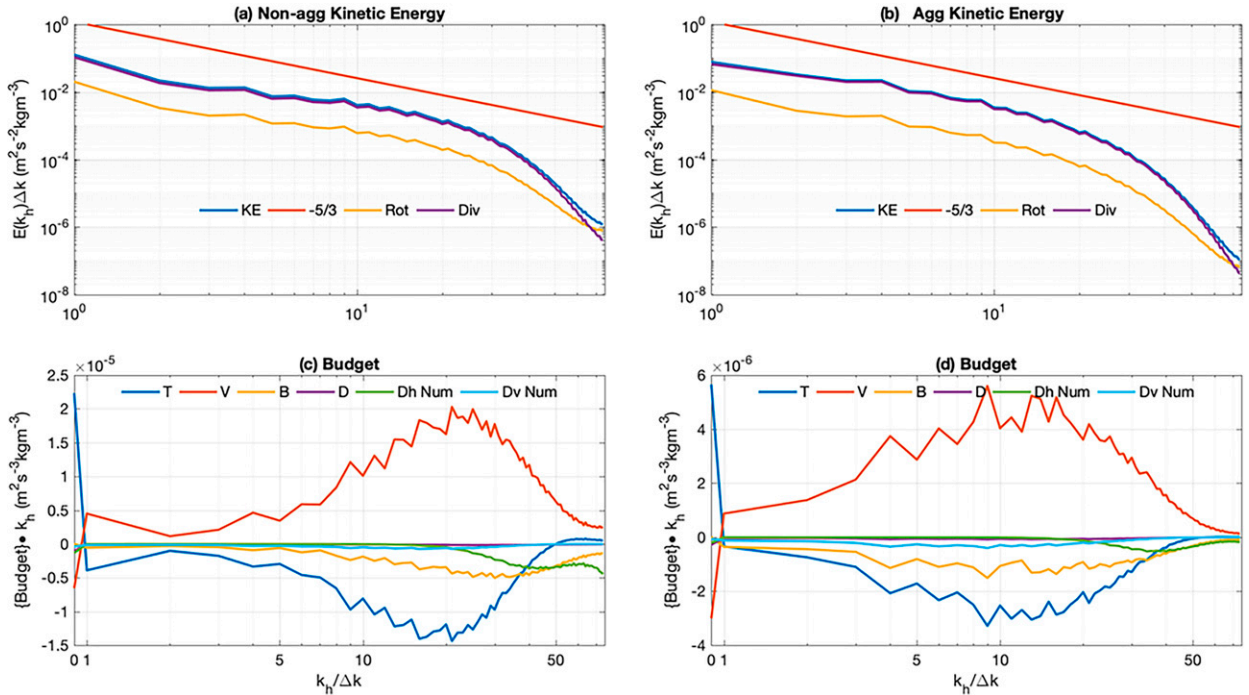
FIG. 6. As in Fig. 4, but in the lower stratosphere (15.5–17 km).

$k_h = 0$ is the only wavenumber at which $T(k_h)$ is significantly larger than zero. As a result, the upscale transfer in the lower stratosphere corresponds to transfer directly into the horizontal mean flow with $k_h = 0$, rather than a turbulent inverse cascade into eddies of large but finite scales, as in two-dimensional and quasigeostrophic turbulence.

An inverse cascade in the lower stratosphere has also been reported by Peng et al. (2015a), Sun et al. (2017), and Menchaca and Durran (2019). Sun et al. (2017) found energy transferred out of small convective scales to larger scales, but it is not clear whether it is going into their mean flow or not. Unlike our transfer, transfers in Peng et al. (2015a) and Menchaca and Durran (2019) are mainly into small nonzero k_h. Notably, both of these simulations had rotation. Peng et al. (2015a) found inverse transfer from 200 to 3000 km and Menchaca and Durran (2019) found that inverse cascade can exist from 90 to 1500 km in their two mountain simulations. The inverse cascade in Menchaca and Durran (2019) occurred with flow over mountains, in which a significant amount of gravity waves were generated in the mesoscale. The fact that the inverse cascade was associated to gravity waves in their finding is similar to ours. As suggested by the vertical energy flux in our budgets (Figs. 6c,d) from the lower stratosphere, our lower stratospheres are dominated by waves as well. Note that in their simulation with no mountains, there was forward cascade instead of inverse cascade.

Inspired by the Eliassen–Palm (EP) flux discussion in Menchaca and Durran (2019), we would like to relate the transfer term at $k_h = 0$ to the rate of change of the mean-flow kinetic energy, which is given by the sum of the following two equations:

$$\frac{\overline{\rho}}{2}\frac{\partial \overline{u}^2}{\partial t} = -\overline{u}\frac{\partial \overline{\rho u' w'}}{\partial z} - \overline{u}\frac{\partial \rho \overline{u}\,\overline{w}}{\partial z}, \qquad (31)$$

$$\frac{\overline{\rho}}{2}\frac{\partial \overline{v}^2}{\partial t} = -\overline{v}\frac{\partial \overline{\rho v' w'}}{\partial z} - \overline{v}\frac{\partial \rho \overline{v}\,\overline{w}}{\partial z}, \qquad (32)$$

where $\overline{(\cdot)}$ represents the horizontal average and $(\cdot)'$ represents the perturbed state from the horizontal average. The first term on the right is the contribution from eddies or the EP flux and the second term on the right is the contribution from the mean flow. Note that the equations above neglect dissipation because we are interested in the wave–mean-flow interaction and the mean-flow interaction here.

The horizontal mean-flow kinetic energy also can be expressed using the advection terms in the spectral budget at $k_h = 0$, which can be further decomposed into the contribution from the transfer term and from part of the vertical flux term:

$$\frac{\overline{\rho}}{2}\frac{\partial \overline{u}^2}{\partial t} + \frac{\overline{\rho}}{2}\frac{\partial \overline{v}^2}{\partial t} = T(0) + V_{\mathrm{adv}}(0)$$

$$= \left(-\overline{u}\frac{\partial \overline{\rho u' w'}}{\partial z} - \overline{v}\frac{\partial \overline{\rho v' w'}}{\partial z} \right) + \left(-\overline{u}\frac{\partial \rho \overline{u}\,\overline{w}}{\partial z} - \overline{v}\frac{\partial \rho \overline{v}\,\overline{w}}{\partial z} \right). \quad (33)$$

Table 1 shows the contribution of EP flux, mean-flow interaction, $T(0)$, and $V_{\mathrm{adv}}(0)$ in the upper troposphere and the lower stratosphere for both simulations. EP fluxes are significantly larger than the mean-flow interaction in all cases. We can further our understanding of the EP flux when we consider $T(0)$ and $V_{\mathrm{adv}}(0)$ as well. In the upper troposphere, the EP flux is dominated by $V_{\mathrm{adv}}(0)$ in both simulations and the contribution from the mean flow is smaller. This suggests that
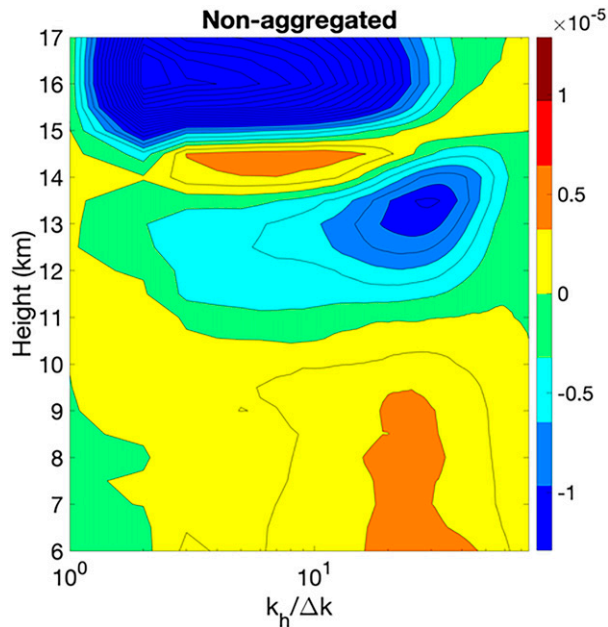
FIG. 7. The nonlinear transfer spectral energy flux $\Pi(k, z)$ ($m^2\ s^{-3}\ kg\ m^{-3}$), which is averaged in time from 841 to 1848 h, from height 6 to 17 km for nonaggregated simulation.

FIG. 8. As in Fig. 7, but for the aggregated simulation.

the mean flow gains energy by vertical energy flux from the advection and the nonlinear transfer term $T(0)$ is not as important as the vertical energy flux in the upper troposphere. In other words, the direct energy cascade found in the upper troposphere does not relate to the wave–mean-flow interaction. In the lower stratosphere, we can see that the EP flux is dominated by $T(0)$ in both simulations. As a result, the fact that $T(0)$ is positive and significant (inverse energy transfer) in the lower stratosphere in both simulations can be explained by the EP flux contribution. Such inflow of energy to the mean flow from the transfer term $T(0)$ in the lower stratosphere is a result of interactions with small-scale waves. Note that while $T(0)$ is stronger, the energy loss of vertical energy flux from the advection for the aggregation is also significant.

d. Compensated kinetic energy spectra

To compare the kinetic energy spectra to observational studies such as Li and Lindborg (2018), one-dimensional (zonal) compensated wavenumber kinetic energy spectra for the nonaggregated and aggregated simulations are computed.
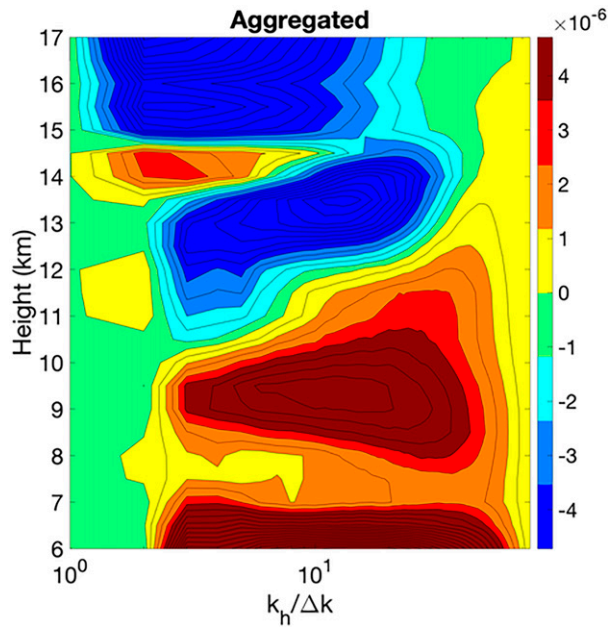
Density dependence is removed to compute k_x spectra of KE per unit mass. One-dimensional compensated spectra are plotted in Fig. 9. These spectra are multiplied by $k_x^{-5/3}$ and plotted on log-linear axes to more carefully compare with a $-5/3$ spectrum. The kinetic energy spectrum from the aggregated simulation is closer to the $-5/3$ spectrum when compared to the nonaggregated simulation in both the upper troposphere and lower stratosphere. The kinetic energy spectrum for the nonaggregated simulation is shallower than $-5/3$ out to $k_x \approx 15$. Even though the slope of the compensated spectrum from the aggregated simulation in the upper troposphere is positive from $k_x = 1$–10, it only increases by a factor of 1.5; by contrast, the compensated kinetic energy spectrum for the nonaggregated simulation increase by a factor of approximately 4–5 for $k_x = 1$–10. The compensated kinetic energy spectrum confirms that DKE is similar to RKE in the upper troposphere and DKE dominates the lower stratosphere for both simulations.

Note that even though there is no baroclinic instability and rotation in our nonaggregated and aggregated idealized simulations, the magnitudes of our compensated kinetic energy spectra are similar to spectra calculated from aircraft data in Li and Lindborg (2018) Fig. 4. They also showed that all of their compensated

TABLE 1. The Eliassen–Palm flux contribution ($m^2\ s^{-3}\ kg\ m^{-3}$), mean-flow contribution ($m^2\ s^{-3}\ kg\ m^{-3}$), transfer at $k_h = 0$ ($m^2\ s^{-3}\ kg\ m^{-3}$), and vertical flux from the advection at $k_h = 0$ ($m^2\ s^{-3}\ kg\ m^{-3}$) for the upper troposphere and the lower stratosphere.

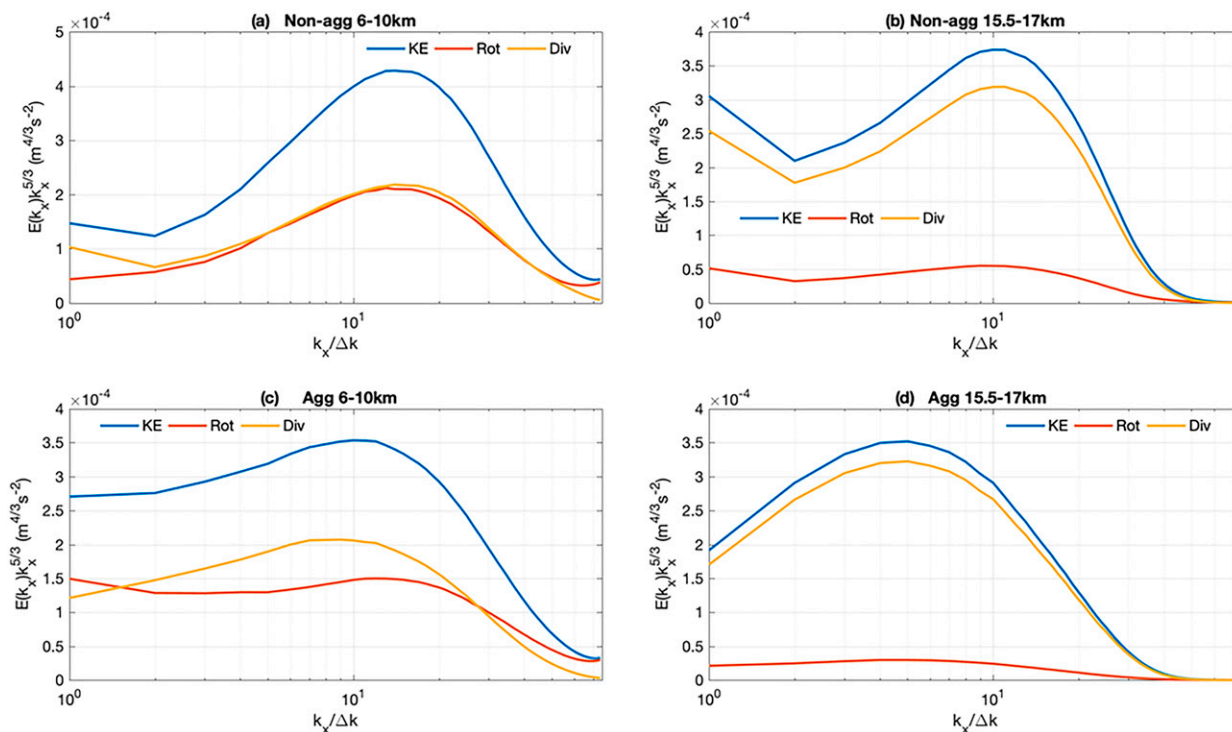| Simulation	EP-flux	Mean-flow interaction	$T(0)$	$V(0)$ from advection
The upper troposphere (6–10 km)				
Nonagg	1.99×10^{-6}	-2.60×10^{-8}	-2.68×10^{-7}	5.17×10^{-7}
Agg	2.92×10^{-7}	5.08×10^{-10}	-1.02×10^{-8}	7.31×10^{-8}
The lower stratosphere (15.5–17 km)				
Nonagg	2.59×10^{-5}	4.99×10^{-9}	2.48×10^{-5}	-7.26×10^{-6}
Agg	5.41×10^{-6}	9.42×10^{-9}	6.28×10^{-6}	-3.34×10^{-6}

FIG. 9. The compensated kinetic energy spectrum for the nonaggregated simulation (a) in the upper troposphere and (b) in the lower stratosphere, and for the aggregated simulation (c) in the upper troposphere and (d) in the lower stratosphere. All spectra are averaged in the vertical and in time from 841 to 1848 h.

kinetic energy spectra are flat in the mesoscale, which suggested that the spectra were close to the −5/3 spectrum.

e. Rotation

The effect of rotation is briefly examined in this subsection. An additional simulation with rotation is run for 42 days and results are averaged for the last 7 days. The setup of the simulation is the same as the nonaggregated simulation, except for the inclusion of midlatitude rotation ($f = 10^{-4}$ s^{-1}). With the addition of rotation, aggregation is identified in the simulation at about 640 h. The convective system looks similar to the aggregated simulation and remains aggregated in the remaining simulation time. In the upper troposphere, the kinetic energy spectrum resembles the −3 spectrum from $k_h = 6$ to $k_h = 20$ (Fig. 10a) in the rotation simulation. This is different from other studies such as the rotation simulation from Sun et al. (2017) and observation from Callies et al. (2014), which found that kinetic energy has a −5/3 spectrum at the mesoscale in the upper troposphere. In Sun et al. (2017), the simulation time was significantly shorter and there was low-level wind shear. The fact that our simulations are much longer allows time for energetic large-scale vortices to develop. In addition, the absence of imposed low-level shear in our simulations may result in different vertical structures. These two factors may explain the steeper spectrum in our study. With the addition of rotation, RKE dominates the kinetic energy spectrum for $k_h < 10$. DKE is marginally stronger than RKE from $k_h = 10$ to $k_h = 50$. The DKE spectrum is shallower, similar to −5/3,

and so it eventually crosses the RKE spectrum, leading to marginally stronger DKE at $k_h > 10$, which is similar to other studies (e.g., Waite and Snyder 2013). In the aggregated and nonaggregated simulations without rotation, RKE and DKE are similar in magnitude for most k_h. The kinetic energy spectrum from the simulation with rotation is also more energetic than the simulations without rotation. The fact that RKE ≳ DKE in the upper troposphere in the rotation simulation is similar to the findings from other studies such as Waite and Snyder (2013) and Peng et al. (2015b).

In the upper troposphere, the energy gain from the buoyancy flux is mainly balanced by the loss of energy from the vertical energy flux for $k_h \lesssim 10$ in the rotation simulation. For $k_h \approx 10$ to 20, there is energy gain from the vertical energy flux that is balanced by the energy loss from the buoyancy flux. The transfer term plays a more significant role in the rotation simulation in the upper troposphere. In the simulations without rotation, the transfer term is weak in the upper troposphere. The transfer term in the rotation simulation transfers energy from large scales to small scales. Energy is dissipated by the dissipation terms at small scales.

In the lower stratosphere, the kinetic energy spectrum is steeper than −5/3 but shallower than −3. The kinetic energy spectrum for the rotation simulation in the lower stratosphere is dominated by RKE for $k_h \lesssim 2$ and dominated by DKE for $k_h > 2$. Note that this is very different from the simulations without rotation. In the simulation without rotation, the kinetic energy spectra for both simulations are dominated by DKE.
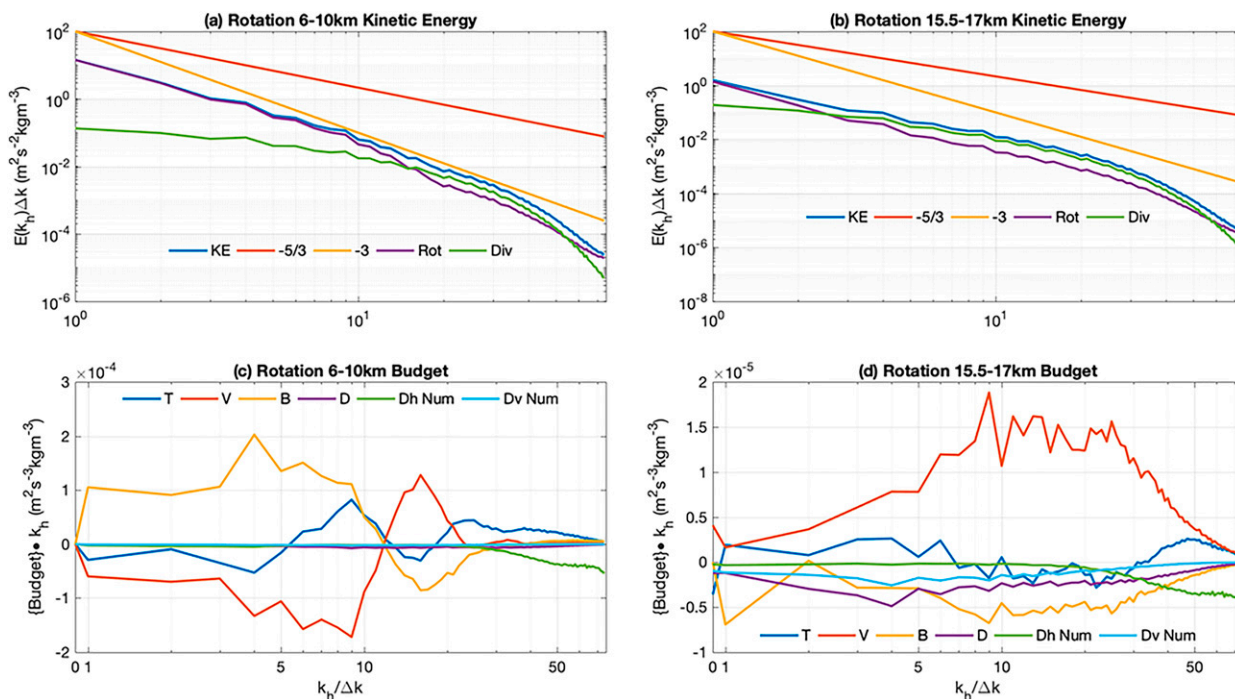
FIG. 10. The horizontal kinetic energy spectrum (blue), rotational kinetic energy spectrum (purple), and divergent kinetic energy spectrum (green) for (a) the upper troposphere (6–10 km) of the rotation simulation and (b) the lower stratosphere (15.5–17 km) of the rotation simulation; and the spectral budget, including horizontal nonlinear energy transfer (blue), buoyancy flux (yellow), vertical flux divergence (red), dissipation from the subgrid mixing scheme (purple), and numerical dissipation (green), in the upper troposphere for (c) the upper troposphere (6–10 km) of the rotation simulation and (d) the lower stratosphere (15.5–17 km) of the rotation simulation. All spectra are averaged in the vertical and in time from 841 to 1008 h. Budget spectra are multiplied by k_h, for all k_h except for $k_h = 0$, to preserve area on semilog plots. Note that $k_h = 0$ is shown in (c) and (d).

In the lower stratosphere, there is a strong energy gain from the vertical energy flux for all k_h in the rotation simulation. It is balanced by energy loss from buoyancy and dissipation. The transfer term is transferring energy out of intermediate scales into larger and smaller scales. Note that the dissipation from the subgrid turbulence scheme is significant even at large scales. The vertical resolution stretches significantly as height increases above 12 km. In our simulations, the vertical resolution at height below 10 km is fairly close to 100 m. The vertical resolution at 15.5 km is approximately 120 m and the vertical resolution at 17 km is approximately 140 m. Low vertical resolution might be leading to significant dissipation at large horizontal scales from vertical gradients (however, this large-scale dissipation was not observed in the simulations without rotation). We decided to keep the same vertical resolution in the rotating case to facilitate comparisons with the nonrotating simulations. It is worth noting that the nonnegligible dissipation at large scales in the lower stratosphere has also been reported in Fig. 9 of Menchaca and Durran (2019).

4. Conclusions

Aggregation in RCE has an impact on the kinetic energy spectrum. In the upper troposphere, the horizontal kinetic energy spectrum is much shallower than the −5/3 spectrum for the nonaggregated simulation. The spectrum for the aggregated simulation is much steeper than the spectrum for the nonaggregated simulation and closer to the −5/3 spectrum. This difference is consistent with the convective system being more energetic in the large scales for the aggregated simulation. In the upper troposphere, DKE is similar to RKE at most scales for the nonaggregated simulation and DKE is slightly larger than RKE for $k_h < 30$ (wavelengths larger than 20 km) in the aggregated simulation. The significant DKE at all scales is likely because of the fact that there is no rotation or large-scale baroclinic instability in our study. The lack of rotation leads to the domination of the DKE in the nonaggregated and aggregated simulation, as confirmed by the simulation with rotation. The addition of rotation was found to facilitate aggregation and development of a −3 spectrum dominated by RKE, in line with other studies.

In the upper troposphere, there is energy gain from the buoyancy flux for both the aggregated and nonaggregated simulation. Buoyancy flux due to latent heating from the convection injects energy into the upper troposphere. In both the nonaggregated and aggregated simulation, the energy gain from buoyancy flux is balanced by energy loss from the vertical energy flux for $k_h < 30$. In the upper troposphere for both simulations, the transfer term transfers some energy from large to small scales and that energy is dissipated, which is consistent with a direct energy cascade.

In the lower stratosphere, the horizontal kinetic energy spectrum is shallower than $-5/3$ and steepens at larger k_h from dissipation. The horizontal kinetic energy spectrum for the aggregated simulation resembles the $-5/3$ spectrum for $4 < k_h < 20$. DKE dominates the horizontal kinetic energy spectrum at all k_h for both simulations. The spectral budgets for both the aggregated and nonaggregated simulations are similar in shape but different in magnitude. The vertical energy flux injects energy to the lower stratosphere and this energy gain is balanced by energy loss from the buoyancy flux, the transfer term, and the dissipation at most scales. Note that the sum of the transfer term has to be zero. The energy loss at $k_h > 1$ is transferred upscale and results in energy gain in the mean flow, which suggests that inverse energy transfer exists in the lower stratosphere. This upscale energy transfer energizes the mean flow in the lower stratosphere, which can be explained by the Eliassen–Palm wave–mean-flow analysis. The transfer of energy to the mean flow in the lower stratosphere is likely due to interactions with small-scale waves. Strong wave activity in the lower stratosphere triggers the wave–mean-flow interaction, and hence energy is transferred from small scales to the mean flow. This may suggest that wave–mean-flow interaction may be responsible for the inverse energy transfer in the lower stratosphere, but not necessarily the same kind of energy cascade/transfer found in inertial-gravity waves and strongly stratified turbulence in explaining the $-5/3$ spectrum.

Even without large-scale forcing and rotation in our nonaggregated and aggregated simulations, the magnitudes of our compensated kinetic energy spectra are similar to spectra calculated from aircraft data. Our results show that latent heating and radiative cooling, through buoyancy and vertical energy fluxes, can force a KE spectrum that resembles a $-5/3$ power law. This spectrum is not due to a turbulent cascade; the role of the nonlinear advective transfer is relatively insignificant. These results serve as a caution that care should be taken when making interpretations about dynamics from the shape of the KE spectrum alone. Note that aggregation does not seem to be an inverse cascade; it results from the buoyancy flux and the vertical energy flux, not the transfer.

In this work, we use model simulations to explore different phenomena and mechanisms that govern the mesoscale energy spectrum. These phenomena and mechanisms are present in the real atmosphere, and idealized simulations allow us to isolate them. RCE experiments focus on dynamics driven by convection, in contrast to previous idealized studies that have focused on, for example, stratified turbulence (Lindborg 2006) and baroclinic instability (Waite and Snyder 2009). We show that RCE develops an energetic mesoscale from a spectral budget that is not an energy cascade, but rather a balance between buoyancy flux and vertical flux. The implication of these results is that in regions dominated by convection, the mesoscale spectrum develops differently than a turbulent cascade.

Future work should focus on the effect of domain size and more carefully identifying gravity waves. Due to the computational expense, it is difficult to run long RCE simulations with a larger domain or higher resolution. Limited domain size may affect our results, and presents a challenge for comparisons with other studies at larger scales. The energy transfer to the mean flow should be investigated with a larger domain. Note that in Peng et al. (2015b) and Menchaca and Durran (2019), the domain size of their simulation was significantly larger than the simulations we presented and rotation was present. This suggests that an inverse energy cascade may exist at scale as large as $O(1000)$ km, at least in the presence of rotation. While we suggest that wave activity may lead to energy transfer from small to large scales, more investigation should be performed. In the H500 mountain simulation from Menchaca and Durran (2019), DKE dominated the HKE spectra in the lower stratosphere at scales less than 900 km. Hence, they concluded that IGWs are important in the lower stratosphere and that might be an explanation for the inverse energy transfer. Is there a way to measure wave activity at a particular length scale? There is a need to confirm if wave activity is crucial in explaining the inverse energy transfer found in the lower stratosphere in the future. DKE is one tool but more work is needed to confirm that DKE identifies waves, and how the wave–mean-flow interaction in our work compares to the inverse cascades reported elsewhere.

Data availability statement. Data are available upon request to the corresponding author.

APPENDIX

Modified Equation

When investigating the effect of numerical dissipation for a partial differential equation, the modified equation can be used. The modified equation is a partial differential equation to which the discretization is a better approximation that the original PDE. It takes both the temporal and spatial discretization into consideration. The modified equation for a one-dimensional linear advection equation, discretized as in WRF, will be given in this section. Consider an advection equation $\partial q/\partial t = -U\partial q/\partial x$ with a constant and positive flow velocity of U. The RK3 time-integration scheme used by WRF for the advection (Skamarock et al. 2008) is given by

$$q_i^{n+1} = q_i^n - \frac{U\Delta t}{\Delta x}(q_{i+1/2}^{**} - q_{i-1/2}^{**}), \tag{A1}$$

where

$$q_i^{**} = q_i - \frac{U\Delta t}{2\Delta x}(q_{i+1/2}^{*} - q_{i-1/2}^{*}), \tag{A2}$$

$$q_i^{*} = q_i - \frac{U\Delta t}{3\Delta x}(q_{i+1/2} - q_{i-1/2}). \tag{A3}$$

For horizontal advection, a fifth-order discretization for $q_{i-1/2}$ is used:

$$q_{i-1/2} = (q^{\mathrm{adv}})^{\mathrm{6th}}_{i-(1/2)} - \frac{1}{60}[(q_{i+2} - q_{i-3})$$
$$- 5(q_{i+1} - q_{i-2}) + 10(q_i - q_{i-1})], \qquad (A4)$$

where $(q^{\mathrm{adv}})^{\mathrm{6th}}_{i-1/2}$ is the sixth-order flux:

$$(q^{\mathrm{adv}})^{\mathrm{6th}}_{i-1/2} = \frac{37}{60}(q_i + q_{i-1}) - \frac{2}{15}(q_{i+1} + q_{i-2})$$
$$+ \frac{1}{60}(q_{i+2} + q_{i-3}). \qquad (A5)$$

Letting $\mathrm{Cr} = U\Delta t/\Delta x$, we can substitute the flux in (A4) in (A1)–(A3), then Taylor expand to obtain

$$\frac{\partial q}{\partial t} + \frac{\Delta t}{2!}\frac{\partial^2 q}{\partial t^2} + \frac{\Delta t^2}{3!}\frac{\partial^3 q}{\partial t^3} + \frac{\Delta t^3}{4!}\frac{\partial^4 q}{\partial t^4} + \frac{\Delta t^4}{5!}\frac{\partial^5 q}{\partial t^5} + \frac{\Delta t^5}{6!}\frac{\partial^6 q}{\partial t^6}$$
$$= -U\frac{\partial q}{\partial x} + \frac{1}{\Delta t}\left[\frac{\mathrm{Cr}}{60}\Delta x^6\frac{\partial^6 q}{\partial x^6} + \frac{\mathrm{Cr}^2}{2}\left(\Delta x^2\frac{\partial^2 q}{\partial x^2}\right) - \frac{\mathrm{Cr}^3}{3!}\left(\Delta x^3\frac{\partial^3 q}{\partial x^3}\right)\right]$$
$$+ \text{h.o.}, \qquad (A6)$$

where h.o. represents the sixth-order terms.

The modified equation for the horizontal advection can be obtained by repeatedly differentiating (A6) to replace time derivatives with spatial derivatives (as in, e.g., Durran 2010):

$$\frac{\partial q}{\partial t} + U\frac{\partial q}{\partial x} = \left(\frac{\mathrm{Cr}}{60\Delta t}\Delta x^6 - \frac{U\mathrm{Cr}^5\Delta x^5}{72}\right)\frac{\partial^6 q}{\partial x^6}$$
$$- \frac{U\mathrm{Cr}^3\Delta x^3}{24}\frac{\partial^4 q}{\partial x^4} - \frac{U\mathrm{Cr}^4\Delta x^4}{30}\frac{\partial^5 q}{\partial x^5} + \text{h.o.} \qquad (A7)$$

Note that the third term on the right side of (A7) is dispersive and the first and second term on the right side of (A7) are dissipative. Similarly, letting $\mathrm{Cr} = W\Delta t/\Delta z$, the modified equation for the vertical advection (Skamarock et al. 2008) is

$$\frac{\partial q}{\partial t} + W\frac{\partial q}{\partial z} = \frac{-\mathrm{Cr}}{12\Delta t}\Delta z^4\frac{\partial^4 q}{\partial z^4} - \frac{W\mathrm{Cr}^3\Delta z^3}{24}\frac{\partial^4 q}{\partial z^4} + \text{h.o.}, \qquad (A8)$$

where h.o. represents the terms that are $O(\Delta z^4)$. Note that the first two terms in (A8) are dissipative. The horizontal numerical dissipation and vertical numerical dissipation presented are defined using the first two terms of (A7) and (A8), respectively.

REFERENCES

Augier, P., and E. Lindborg, 2013: A new formulation of the spectral energy budget of the atmosphere, with application to two high-resolution general circulation models. *J. Atmos. Sci.*, **70**, 2293–2308, https://doi.org/10.1175/JAS-D-12-0281.1.

Becker, T., B. Stevens, and C. Hohenegger, 2017: Imprint of the convective parameterization and sea-surface temperature on large-scale convective self-aggregation. *J. Adv. Model. Earth Syst.*, **9**, 1488–1505, https://doi.org/10.1002/2016MS000865.

Bretherton, C. S., P. N. Blossey, and M. Khairoutdinov, 2005: An energy-balance analysis of deep convective self-aggregation above uniform SST. *J. Atmos. Sci.*, **62**, 4273–4292, https://doi.org/10.1175/JAS3614.1.

Bryan, G. H., and H. Morrison, 2012: Sensitivity of a simulated squall line to horizontal resolution and parameterization of microphysics. *Mon. Wea. Rev.*, **140**, 202–225, https://doi.org/10.1175/MWR-D-11-00046.1.

——, J. C. Wyngaard, and J. M. Fritsch, 2003: Resolution requirements for the simulation of deep moist convection. *Mon. Wea. Rev.*, **131**, 2394–2416, https://doi.org/10.1175/1520-0493(2003)131<2394:RRFTSO>2.0.CO;2.

Callies, J., R. Ferrari, and O. Bühler, 2014: Transition from geostrophic turbulence to inertia–gravity waves in the atmospheric energy spectrum. *Proc. Natl. Acad. Sci. USA*, **111**, 17 033–17 038, https://doi.org/10.1073/pnas.1410772111.

——, O. Bühler, and R. Ferrari, 2016: The dynamics of mesoscale winds in the upper troposphere and lower stratosphere. *J. Atmos. Sci.*, **73**, 4853–4872, https://doi.org/10.1175/JAS-D-16-0108.1.

Charney, J. G., 1971: Geostrophic turbulence. *J. Atmos. Sci.*, **28**, 1087–1095, https://doi.org/10.1175/1520-0469(1971)028<1087:GT>2.0.CO;2.

Cho, J. Y., and E. Lindborg, 2001: Horizontal velocity structure functions in the upper troposphere and lower stratosphere: 1. Observations. *J. Geophys. Res.*, **106**, 10 223–10 232, https://doi.org/10.1029/2000JD900814.

——, and Coauthors, 1999: Horizontal wavenumber spectra of winds, temperature, and trace gases during the Pacific Exploratory Missions: 1. Climatology. *J. Geophys. Res.*, **104**, 5697–5716, https://doi.org/10.1029/98JD01825.

Colin, M., S. Sherwood, O. Geoffroy, S. Bony, and D. Fuchs, 2019: Identifying the sources of convective memory in cloud-resolving simulations. *J. Atmos. Sci.*, **76**, 947–962, https://doi.org/10.1175/JAS-D-18-0036.1.

Durran, D. R., 2010: *Numerical Methods for Fluid Dynamics: With Applications to Geophysics*. Vol. 32. Springer Science and Business Media, 533 pp.

Hamilton, K., Y. O. Takahashi, and W. Ohfuchi, 2008: Mesoscale spectrum of atmospheric motions investigated in a very fine resolution global general circulation model. *J. Geophys. Res.*, **113**, D18110, https://doi.org/10.1029/2008JD009785.

Holloway, C. E., and S. J. Woolnough, 2016: The sensitivity of convective aggregation to diabatic processes in idealized radiative-convective equilibrium simulations. *J. Adv. Model. Earth Syst.*, **8**, 166–195, https://doi.org/10.1002/2015MS000511.

Jeevanjee, N., and D. M. Romps, 2013: Convective self-aggregation, cold pools, and domain size. *Geophys. Res. Lett.*, **40**, 994–998, https://doi.org/10.1002/grl.50204.

Jiménez, P. A., J. Dudhia, J. F. González-Rouco, J. Navarro, J. P. Montávez, and E. García-Bustamante, 2012: A revised scheme for the WRF surface layer formulation. *Mon. Wea. Rev.*, **140**, 898–918, https://doi.org/10.1175/MWR-D-11-00056.1.

Kolmogorov, A. N., 1941: The local structure of turbulence in incompressible viscous fluid for very large Reynolds numbers. *Proc. Roy. Soc. London*, **434A**, 9–13, http://doi.org/10.1098/rspa.1991.0075.

Li, Q., and E. Lindborg, 2018: Weakly or strongly nonlinear mesoscale dynamics close to the tropopause? *J. Atmos. Sci.*, **75**, 1215–1229, https://doi.org/10.1175/JAS-D-17-0063.1.

Lilly, D. K., 1983: Stratified turbulence and the mesoscale variability of the atmosphere. *J. Atmos. Sci.*, **40**, 749–761, https://doi.org/10.1175/1520-0469(1983)040<0749:STATMV>2.0.CO;2.

Lindborg, E., 2006: The energy cascade in a strongly stratified fluid. *J. Fluid Mech.*, **550**, 207–242, https://doi.org/10.1017/S0022112005008128.

Malardel, S., and N. P. Wedi, 2016: How does subgrid-scale parametrization influence nonlinear spectral energy fluxes in global NWP models? *J. Geophys. Res. Atmos.*, **121**, 5395–5410, https://doi.org/10.1002/2015JD023970.

Menchaca, M. Q., and D. R. Durran, 2019: The influence of gravity waves on the slope of the kinetic energy spectrum in simulations of idealized midlatitude cyclones. *J. Atmos. Sci.*, **76**, 2103–2122, https://doi.org/10.1175/JAS-D-18-0329.1.

Muller, C. J., and I. M. Held, 2012: Detailed investigation of the self-aggregation of convection in cloud-resolving simulations. *J. Atmos. Sci.*, **69**, 2551–2565, https://doi.org/10.1175/JAS-D-11-0257.1.

——, and S. Bony, 2015: What favors convective aggregation and why? *Geophys. Res. Lett.*, **42**, 5626–5634, https://doi.org/10.1002/2015GL064260.

Nastrom, G. D., and K. S. Gage, 1985: A climatology of atmospheric wavenumber spectra of wind and temperature observed by commercial aircraft. *J. Atmos. Sci.*, **42**, 950–960, https://doi.org/10.1175/1520-0469(1985)042<0950:ACOAWS>2.0.CO;2.

Nolan, D. S., E. D. Rappin, and K. A. Emanuel, 2007: Tropical cyclogenesis sensitivity to environmental parameters in radiative–convective equilibrium. *Quart. J. Roy. Meteor. Soc.*, **133**, 2085–2107, https://doi.org/10.1002/qj.170.

Peng, J., L. Zhang, Y. Luo, and Y. Zhang, 2014: Mesoscale energy spectra of the mei-yu front system. Part I: Kinetic energy spectra. *J. Atmos. Sci.*, **71**, 37–55, https://doi.org/10.1175/JAS-D-13-085.1.

——, ——, and J. Guan, 2015a: Applications of a moist nonhydrostatic formulation of the spectral energy budget to baroclinic waves. Part I: The lower-stratospheric energy spectra. *J. Atmos. Sci.*, **72**, 2090–2108, https://doi.org/10.1175/JAS-D-14-0306.1.

——, ——, and ——, 2015b: Applications of a moist nonhydrostatic formulation of the spectral energy budget to baroclinic waves. Part II: The upper-tropospheric energy spectra. *J. Atmos. Sci.*, **72**, 3923–3939, https://doi.org/10.1175/JAS-D-14-0359.1.

Reed, K. A., and B. Medeiros, 2016: A reduced complexity framework to bridge the gap between AGCMs and cloud-resolving models. *Geophys. Res. Lett.*, **43**, 860–866, https://doi.org/10.1002/2015GL066713.

Robe, F. R., and K. A. Emanuel, 2001: The effect of vertical wind shear on radiative–convective equilibrium states. *J. Atmos. Sci.*, **58**, 1427–1445, https://doi.org/10.1175/1520-0469(2001)058<1427:TEOVWS>2.0.CO;2.

Rotunno, R., and K. A. Emanuel, 1987: An air–sea interaction theory for tropical cyclones. Part II: Evolutionary study using a nonhydrostatic axisymmetric numerical model. *J. Atmos. Sci.*, **44**, 542–561, https://doi.org/10.1175/1520-0469(1987)044<0542:AAITFT>2.0.CO;2.

Satoh, M., and Y. Matsuda, 2009: Statistics on high-cloud areas and their sensitivities to cloud microphysics using single-cloud experiments. *J. Atmos. Sci.*, **66**, 2659–2677, https://doi.org/10.1175/2009JAS2948.1.

Skamarock, W. C., 2004: Evaluating mesoscale NWP models using kinetic energy spectra. *Mon. Wea. Rev.*, **132**, 3019–3032, https://doi.org/10.1175/MWR2830.1.

——, and Coauthors, 2008: A description of the Advanced Research WRF version 3. NCAR Tech. Note NCAR/TN-475+STR, 113 pp., https://doi.org/10.5065/D68S4MVH.

——, S.-H. Park, J. B. Klemp, and C. Snyder, 2014: Atmospheric kinetic energy spectra from global high-resolution nonhydrostatic simulations. *J. Atmos. Sci.*, **71**, 4369–4381, https://doi.org/10.1175/JAS-D-14-0114.1.

Smagorinsky, J., 1963: General circulation experiments with the primitive equations: I. The basic experiment. *Mon. Wea. Rev.*, **91**, 99–164, https://doi.org/10.1175/1520-0493(1963)091<0099:GCEWTP>2.3.CO;2.

Sun, Y. Q., R. Rotunno, and F. Zhang, 2017: Contributions of moist convection and internal gravity waves to building the atmospheric $-5/3$ kinetic energy spectra. *J. Atmos. Sci.*, **74**, 185–201, https://doi.org/10.1175/JAS-D-16-0097.1.

Thompson, G., P. R. Field, R. M. Rasmussen, and W. D. Hall, 2008: Explicit forecasts of winter precipitation using an improved bulk microphysics scheme. Part II: Implementation of a new snow parameterization. *Mon. Wea. Rev.*, **136**, 5095–5115, https://doi.org/10.1175/2008MWR2387.1.

Tompkins, A. M., and A. G. Semie, 2017: Organization of tropical convection in low vertical wind shears: Role of updraft entrainment. *J. Adv. Model. Earth Syst.*, **9**, 1046–1068, https://doi.org/10.1002/2016MS000802.

Tulloch, R., and K. S. Smith, 2009: Quasigeostrophic turbulence with explicit surface dynamics: Application to the atmospheric energy spectrum. *J. Atmos. Sci.*, **66**, 450–467, https://doi.org/10.1175/2008JAS2653.1.

Tung, K. K., and W. W. Orlando, 2003: The k^{-3} and $k^{-5/3}$ energy spectrum of atmospheric turbulence: Quasigeostrophic two-level model simulation. *J. Atmos. Sci.*, **60**, 824–835, https://doi.org/10.1175/1520-0469(2003)060<0824:TKAKES>2.0.CO;2.

Vallis, G., 2006: *Atmospheric and Oceanic Fluid Dynamics: Fundamentals and Large-Scale Circulation*. Cambridge University Press, 769 pp.

VanZandt, T., 1982: A universal spectrum of buoyancy waves in the atmosphere. *Geophys. Res. Lett.*, **9**, 575–578, https://doi.org/10.1029/GL009i005p00575.

Waite, M. L., 2016: Dependence of model energy spectra on vertical resolution. *Mon. Wea. Rev.*, **144**, 1407–1421, https://doi.org/10.1175/MWR-D-15-0316.1.

——, and C. Snyder, 2009: The mesoscale kinetic energy spectrum of a baroclinic life cycle. *J. Atmos. Sci.*, **66**, 883–901, https://doi.org/10.1175/2008JAS2829.1.

——, and ——, 2013: Mesoscale energy spectra of moist baroclinic waves. *J. Atmos. Sci.*, **70**, 1242–1256, https://doi.org/10.1175/JAS-D-11-0347.1.

Wing, A. A., and K. A. Emanuel, 2014: Physical mechanisms controlling self-aggregation of convection in idealized numerical modeling simulations. *J. Adv. Model. Earth Syst.*, **6**, 59–74, https://doi.org/10.1002/2013MS000269.

——, and T. W. Cronin, 2016: Self-aggregation of convection in long channel geometry. *Quart. J. Roy. Meteor. Soc.*, **142**, 1–15, https://doi.org/10.1002/qj.2628.

——, K. Emanuel, C. E. Holloway, and C. Muller, 2017: Convective self-aggregation in numerical simulations: A review. *Surv. Geophys.*, **38**, 1173–1197, https://doi.org/10.1007/s10712-017-9408-4.

——, K. A. Reed, M. Satoh, B. Stevens, S. Bony, and T. Ohno, 2018: Radiative–Convective Equilibrium Model Intercomparison Project. *Geosci. Model Dev.*, **11**, 793–813, https://doi.org/10.5194/gmd-11-793-2018.

Wyngaard, J., 2010: *Turbulence in the Atmosphere*. Cambridge University Press, 393 pp.